REPORT
229

# ISOTOPIC FINGERPRINTING OF NATIVE GOLD FROM WESTERN AUSTRALIA

SG Tessalina, EA Hancock, B Ware and NJ McNaughton

John de Laeter Centre

Curtin University

EXPLORATION INCENTIVE SCHEME

Government of Western Australia
Department of Mines, Industry Regulation and Safety

Geological Survey of Western Australia

Government of **Western Australia**
Department of **Mines, Industry Regulation and Safety**

REPORT 229

# ISOTOPIC FINGERPRINTING OF NATIVE GOLD FROM WESTERN AUSTRALIA

SG Tessalina*, EA Hancock, B Ware* and NJ McNaughton*

* John de Laeter Centre, Curtin University, Kent St, Bentley WA 6102

PERTH 2023

**Geological Survey of Western Australia**

**REFERENCE**
**The recommended reference for this publication is:**
Tessalina, SG, Hancock, EA, Ware, B and McNaughton, NJ 2023, Isotopic fingerprinting of native gold from Western Australia: Geological Survey of Western Australia, Report 229, 32p.

**ISBN** 978-1-74168-986-0
**ISSN** 1834-2280

A catalogue record for this book is available from the National Library of Australia

Grid references in this publication refer to the Geocentric Datum of Australia 1994 (GDA94). Locations mentioned in the text are referenced using Map Grid Australia (MGA) coordinates, Zones 50 and 51. All locations are quoted to at least the nearest 100 m.

**Acknowledgement**
This study acknowledges the analytical infrastructure support of the John de Laeter Centre, Curtin University.



**Published 2023 by the Geological Survey of Western Australia**
This Report is published in digital format (PDF) and is available online at <www.dmirs.wa.gov.au/GSWApublications>.



**Further details of geoscience products are available from:**
First Floor Counter
Department of Mines, Industry Regulation and Safety
100 Plain Street, EAST PERTH WESTERN AUSTRALIA 6004
Telephone: +61 8 9222 3459 Email: publications@dmirs.wa.gov.au
**www.dmirs.wa.gov.au/GSWApublications**

**Cover photograph:** Small gold nuggets and gold-bearing samples from Paulsens gold deposit, West Pilbara, Kurnalpi goldfield, Mount Olympus gold deposit, and East Pilbara. These gold samples and their galena micro-inclusions are used for the Pb isotope and trace element analyses

# Contents



## Appendices

*Available with the PDF online as an accompanying digital resource*

1. Sample selection table: brief geological settings and gold nugget characteristics
2. Pb–Pb and Re–Os isotope composition in selected gold samples
3. Trace elements in selected gold samples in solution mode

# Figures



# Tables

# Isotopic fingerprinting of native gold from Western Australia

**SG Tessalina*, EA Hancock, B Ware* and NJ McNaughton***

## Abstract

Native gold has proven to be difficult to characterize geochemically due to its scarcity, small sample size, mono-isotopic nature, and due to the specific protocols and dedicated equipment required to overcome analytical difficulties. Therefore, direct geochemical studies of native gold are sparse and the majority of information about the age and origin of gold deposits comes from associated bedrock and accessory minerals. To address this issue, we investigated 24 small gold nuggets from various locations in Western Australia, including the Pilbara Craton (Silica Hills, Mallina, Marble Bar and Mosquito Creek prospects), Yilgarn Craton (Kurnalpi Terrane), and Capricorn Orogen (Paulsens and Mount Olympus deposits), with the aim of constraining the age and source of gold mineralization directly from gold. The samples were analysed for Pb and Os isotopes, platinum group elements (PGE), and other trace elements using wet chemistry techniques in combination with thermal ionization mass spectrometry (TIMS) and high-resolution inductively coupled plasma mass spectrometry (HR-ICP-MS). We assessed the applicability of these analytical techniques for isotopic and sub-ppm to sub-ppb trace element fingerprinting of native gold samples and gold reference standards.

One of the most important results was establishing reliable Pb–Pb model ages for some gold samples, as well as characterizing the source of Pb prior to mineralization. For the Kurnalpi Terrane, the results indicate that the nuggets are of similar age and composition to known bedrock mineralization in the region, implying a common age and origin. Galena inclusions in gold nuggets from the Kurnalpi Terrane display the most primitive Pb isotope compositions, with Neoarchean model ages ranging from 2.72 to 2.65 Ga, similar to ages of the host rocks. The least radiogenic Pb isotopes from galena inclusions in Pilbara gold yield model ages of 2.25 Ga for Marble Bar, 2.66 – 2.44 Ga for Mosquito Creek and 2.91 – 2.87 Ga for Silica Hills, indicating a more complex history, possibly due to overprinting by younger events, subsequent alteration within regolith, and/or addition of uranium during secondary processes. Gold samples from Capricorn Orogen deposits lack galena inclusions, have primitive Pb isotopes, contain small amounts of U and show no evidence of alteration or overprinting by geological events since their formation. A gold nugget from the Mount Olympus area yielded a model age of 1.66 Ga, which is compatible with the known age of the younger mineralization event at the Paulsens gold mine.

The source μ ($^{238}U/^{204}Pb$) values for galena inclusions and less-altered gold nuggets from the Kurnalpi Terrane range from 8.17 to 8.28, similar to values for volcanogenic massive sulfide deposits at Teutonic Bore and Nimbus (8.1 and 8.4, respectively). These results indicate a mostly juvenile, predominantly mantle-derived source for Pb. The Re–Os systematics of gold reveal a predominantly mantle source of Os, possibly related to magmatic fluid input without significant crustal contamination, which has not been detected previously by other lithophile-based isotope systems. The Re–Os and PGE patterns in placer gold nuggets from the Pilbara appear to preserve their initial source signatures without significant chemical alteration during their burial history.

**KEYWORDS**: fingerprinting, native gold, Pb isotopes, Re–Os isotopes, trace elements

## Introduction

The current project tested the feasibility of direct isotopic dating of native gold and whether chemical fingerprinting of low-level trace elements in native gold could aid the understanding of the gold source and improve exploration success. The project was framed around previously collected and prepared gold nuggets curated with the Geological Survey of Western Australia (GSWA) and included mostly placer nuggets and gold from known gold deposits (Fig. 1).

The project involved technical developments to optimize the efficiency and reliability of data gathering, including sampling protocols. There are a number of challenges in sampling the native gold nuggets: i) the small size of the majority of gold grains available; ii) samples without mineral inclusions; iii) possible contamination during the sampling by sampling tools. There are also challenges related to the analytical techniques: i) working with a small sample amount, which requires efficient extraction of elements of interest; ii) testing for possible contamination by mineral inclusions; iii) managing the 'sticky' behaviour of gold (memory effect) during measurement in solution, requiring a modification of the washing protocol.

Previous isotope studies to determine the age and primary source of gold mineralization have generally focused on coexisting accessory minerals interpreted to have formed from the same ore fluid. These results, even considered together with independently determined regional structural and absolute timing (4D) constraints, typically do not unequivocally determine gold sources or elucidate the timing of processes that generated the gold deposits in their current form.

* John de Laeter Centre, Curtin University, Kent St, Bentley WA 6102

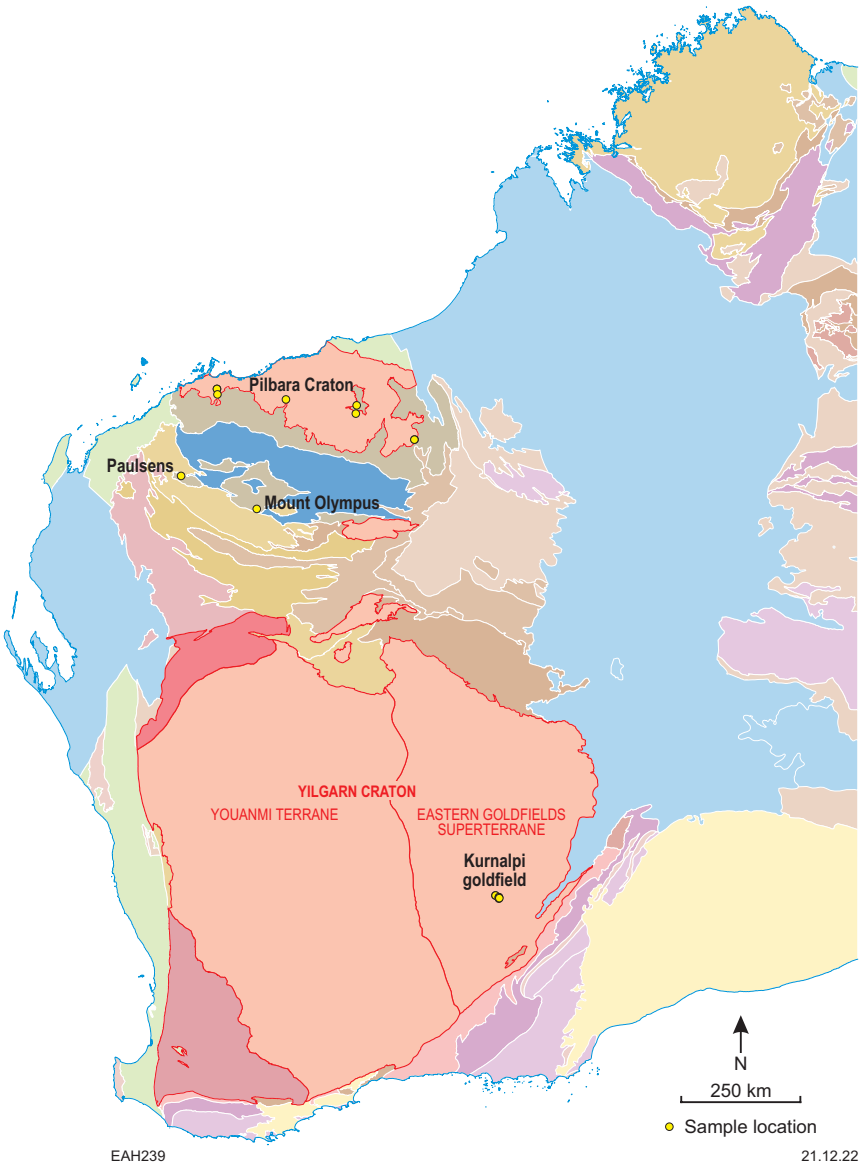


Figure 1. Simplified 1:10 000 000 tectonic unit map of Western Australia, showing gold sample locations

Recent GSWA studies of gold mineralogy and trace element chemistry have aimed to determine primary source and type of mineralization for placer and bedrock gold grains from various locations in Western Australia, including the Capricorn Orogen, Kurnalpi Terrane and Pilbara Craton (Hancock and Thorne, 2011; Hancock and Thorne, 2016; Hancock and Beardsmore, 2020).

In this project, state-of-the-art isotope techniques (Pb–Pb and Re–Os) and trace element analysis (to sub-ppm levels) were applied to previously documented native gold samples to better constrain the timing and sources of gold mineralization in these areas. The analytical studies were conducted in the thermal ionization mass spectrometry (TIMS) node of the John de Laeter Centre (JdLC) at Curtin University using a Triton TIMS and a sector-field high-resolution inductively coupled plasma mass spectrometer (HR-ICP-MS) Element XR.

## Objectives

The main objective of this study was to analyse native gold samples from several locations to assess whether the ultimate source(s) of noble metals, the timing of gold deposition, and associated exploration models can be better constrained.

Specific aims were to:

1. establish procedures for extracting representative samples from native gold grains
2. analyse the trace element abundance (including platinum group elements [PGE] and rare earth elements [REE]) and Pb–Os isotope compositions of native gold samples using TIMS and HR-ICP-MS in solution mode
3. assess the utility of Pb–Os radiogenic isotopes and trace elements for provenance determination and direct dating of native gold from Western Australia.

# Sample selection

Selection of samples for any type for geochemical analysis is one of the most important parts of the study. GSWA stores a collection of native gold samples accumulated since 2009 as part of the gold fingerprinting study. All gold grains in this collection are mounted in resin, and their Ag and trace element composition and microstructure have been analysed using scanning electron microscopy with energy dispersive X-ray system (SEM-EDS) and the electron backscattered diffraction detector, laser ablation inductively coupled plasma mass spectrometry (LA-ICP-MS), and acid etching methods. The results of these analytical characterization techniques are necessary prerequisites to the current study.

Limitations in selecting gold grains for isotope analysis include availability and diversity in the collection, and size and existence of relevant geological, mineralogical and geochemical data. Specific constraints are:

- The availability of gold samples in the GSWA collection require sufficient variability to represent different geological and mineralogical settings.
- The size of selected gold grains must be sufficient to allow (partially) destructive isotope and trace element analyses, while leaving at least half of the gold sample in the collection. Ideally about 100 mg of gold is required for analysis, so the minimum size of the original pure gold grain should be >200 mg, or >10 $mm^3$ (for example, more than 5 × 2 × 1 mm). Some samples used in this study that weighed 2–10 mg did not yield reliable results for some analysed isotopes.
- Visible gold grains are commonly intergrown with other minerals introduced into a gold nugget either during crystallization or later deformation and recrystallization processes. These visible inclusions should be avoided during sampling. The presence of micro-inclusions, previously detected by optical microscopy and SEM, should also be considered during data processing.
- The microstructures of gold grains are mainly heterogeneous, with different phases of crystallization and hypogene and supergene alteration. Ideally, individual phases should be analysed separately, if permitted by their sizes. However, during development of extraction techniques in this study, the majority of analysed samples were found to consist of several gold phases and potential mineral inclusions.
- The availability of LA-ICP-MS geochemical data is an important criterion in sample selection for calibration purposes and to permit selection of high-Pb samples for more accurate Pb–Pb isotope analysis.

A total of 19 gold grains (Fig. 2) have been analysed for Pb–Pb and Re–Os isotopes and trace elements. Full petrographic details of the samples are presented in Appendix 1. The samples are:

- Kurnalpi goldfield (Yilgarn Craton) – GSWA 201929, GSWA 201930, GSWA 201943, GSWA 201954 and GSWA 201962
- Paulsens and Mount Olympus gold deposits (Capricorn Orogen) – GSWA 201909, GSWA 201912 and GSWA 201914
- Silica Hills (West Pilbara) – GSWA 201981 and GSWA 201994
- Marble Bar and Mosquito Creek (East Pilbara) – GSWA 201969 and GSWA 247031.

In addition, six gold samples were used for extraction of galena micro-inclusions for Pb–Pb isotope analysis (Fig. 3; Appendix 1):

- Kurnalpi goldfield (Yilgarn Craton) – GSWA 201941 and GSWA 201943
- Silica Hills (West Pilbara) – GSWA 201978
- Mallina (Central Pilbara) – GSWA 247009
- Marble Bar and Mosquito Creek (East Pilbara) – GSWA 247016 and GSWA 247032.

# Methods

## Sampling

Initial sampling was performed in the GSWA laboratory and involved the use of a dental drill to scratch the sample surface and recover filings (Fig. 4A). The advantage of this sampling method is that the extracted material is relatively pure because it mostly comes from the polished surface and visible inclusions can be avoided. The disadvantages of this method include the large sampling surface, which can include heterogeneous areas of native gold, and the small amount of material recovered.

The weights of 16 samples extracted by this method varied from 2 to 10 mg, with a median of 5 mg. This amount proved too little for high-precision Re–Os and Pb–Pb isotope analysis and was supplemented by hand-drilling larger amounts (Fig. 4B).

## Wet chemistry (dissolution of gold)

To avoid contamination from sampling, the recovered gold samples and reference materials (RM) were acid washed in 50% HCl in an ultrasonic bath, rinsed and ultrasonically cleaned several times in distilled deionized water, and then dried in a clean fume hood.

After washing, about 3 to 10 mg of gold sample was mixed with appropriate amounts of mixed $^{185}Re$–$^{190}Os$ and PGE spike. Acid digestion was carried out using concentrated acids (3 ml of purged double-distilled $HNO_3$ and 1 ml of triple-distilled HCl).

Digestion of samples was conducted using two different methods. The first batch of 2 to 10 mg samples (separated by dental drill), together with gold RM, were digested in Teflon bombs in the oven at 140 °C. The second batch of samples (separated by hand drill) involved larger amounts of material, and was digested in Pyrex borosilicate Carius tubes and heated to 220 °C for 36 hours (Fig. 5).


Figure 2. Gold nuggets selected for isotope and trace element analyses. Descriptions of samples are provided in Appendix 1

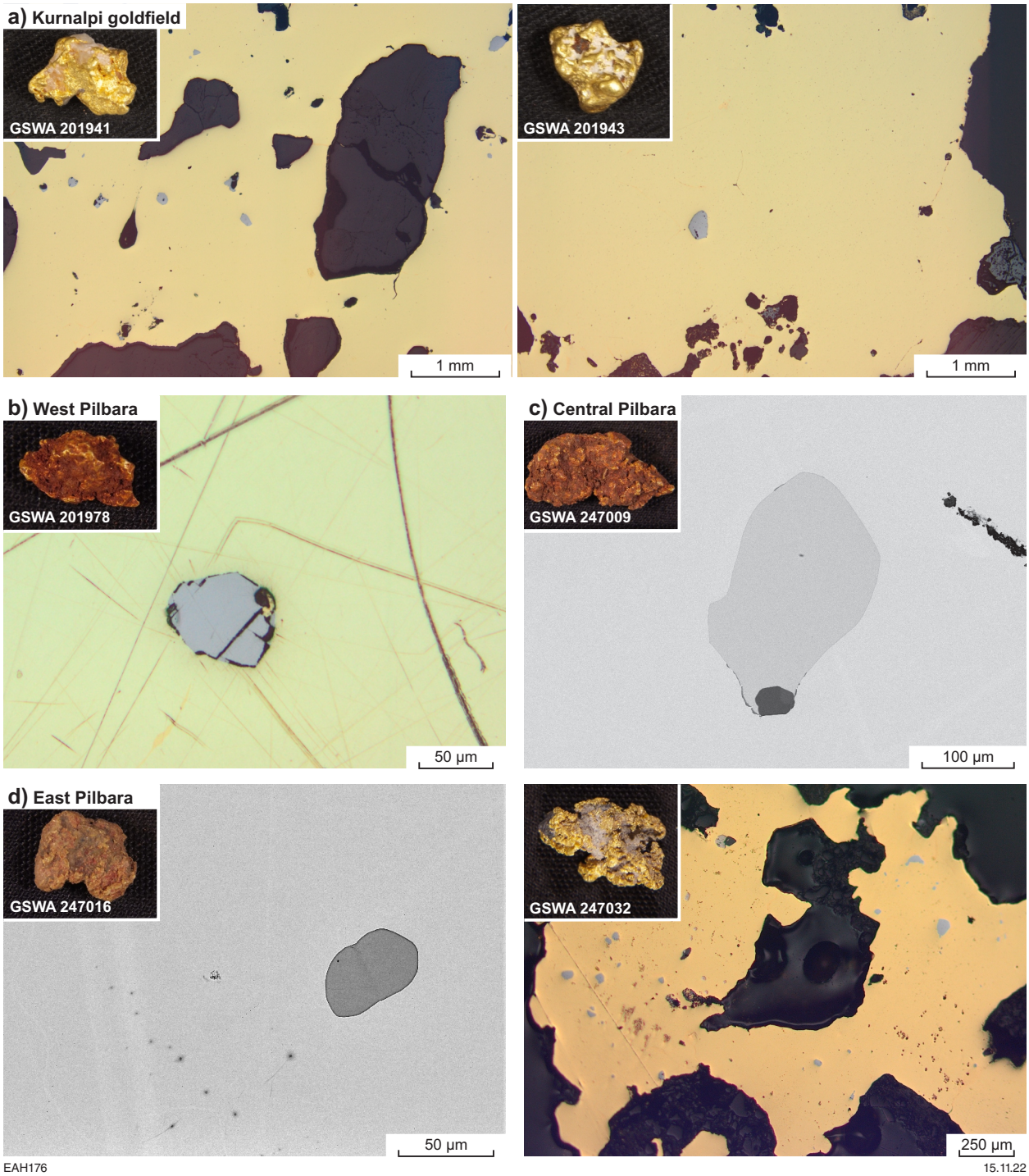


Figure 3. Gold nuggets with galena inclusions selected for isotope analysis. Descriptions of samples are provided in Appendix 1

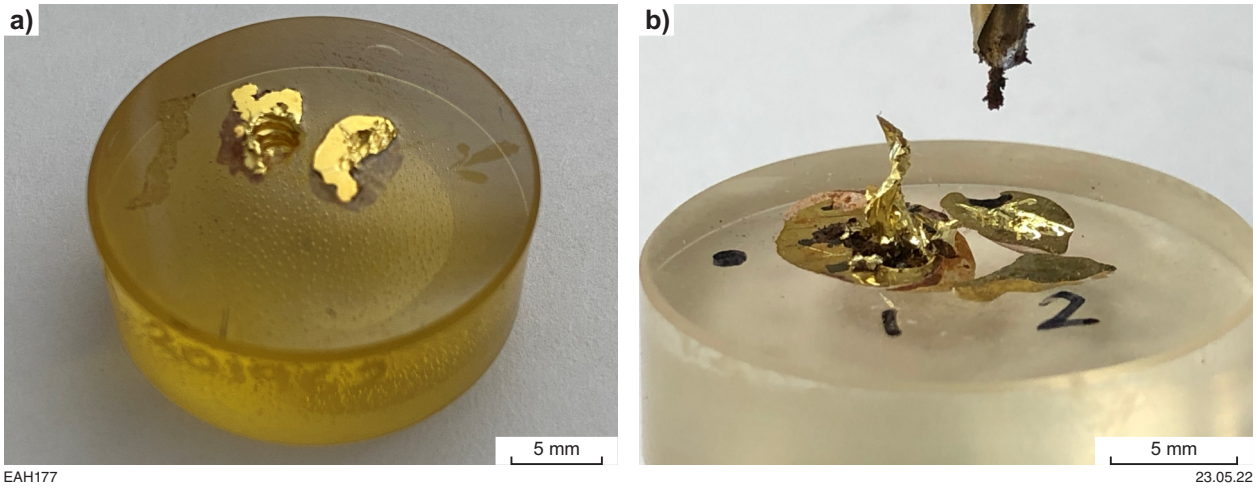


Figure 4. Examples of gold nuggets sampled: a) using a dental drill; b) by hand-drilling

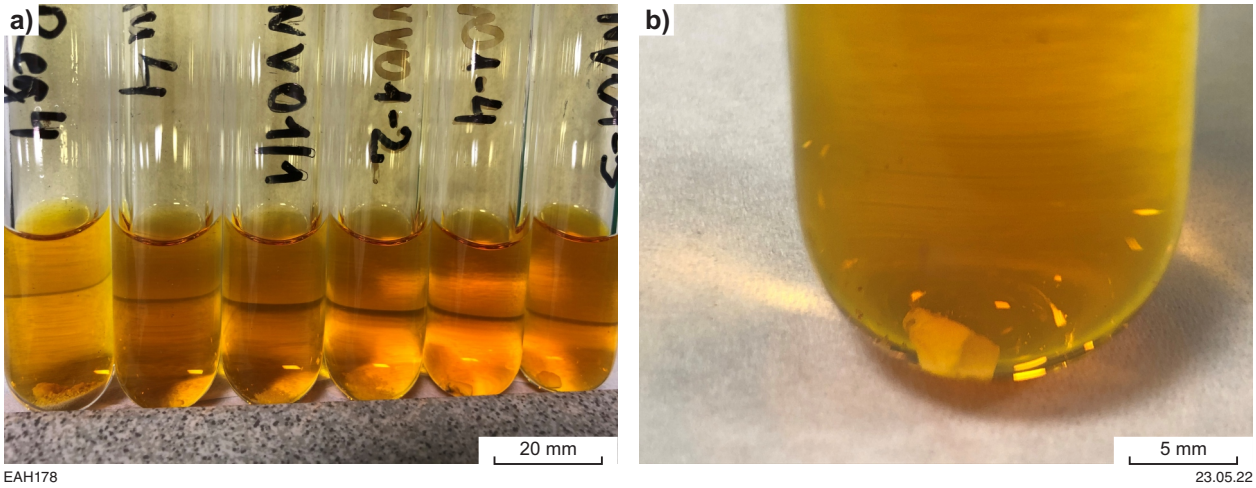


Figure 5. Features of gold samples after Carius tube digestion: a) after digestion in aqua regia for 36 hours at 220 °C; b) remnants of larger gold nuggets are coated by insoluble silver chloride (white) that persists after dissolution

Extraction of Os was carried out first from the resulting solution (see below). The remaining reverse aqua regia solution was dried down on a hot plate, and the residue was redissolved in 6N HCl and then refluxed on a hot plate overnight. Half of this solution was used for Pb chromatography. The remaining half was used for extraction of Re and PGE via anion exchange chromatography, and for trace element analysis. Measurements of Pb and Os isotope compositions were made using a Triton TIMS, and trace elements and PGE abundances were measured in solution mode using an Element HR-ICP-MS.

## Re–Os systematics

The Re and Os concentrations and Os isotope compositions were measured from the sample materials digested using Teflon bombs (Birck et al., 1997) and Carius tubes (Shirey and Walker, 1995). Prior to digestion, a Re–Os tracer solution as well as a PGE tracer solution were weighed and added to each sample. After digestion, Os was extracted from the acid solution by chloroform solvent extraction (Cohen and Waters, 1996), then back-extracted into HBr, followed by purification via microdistillation (Birck et al., 1997). Rhenium was separated from a portion of the residual liquid using anion exchange chromatography, passing the solution through AG1-X8 200–400 mesh anion exchange resin (Eichrom) in a 1N HCl medium with final recovery of Re from the column via 6N $HNO_3$.

The purified Os was loaded onto platinum filaments and measured via negative-ion thermal ionization mass spectrometry (N-TIMS) on a ThermoFisher Triton mass spectrometer using a secondary electron multiplier detector at JdLC. Rhenium was measured in solution using an HR-ICP-MS Element mass spectrometer.

To monitor long-term instrument reproducibility on the Triton TIMS, an AB-2 Os standard (University of Alberta) was analysed during the period of the measurements, and yielded an $^{187}Os/^{188}Os$ isotope ratio of 0.10689 ± 0.00022 ($n$ = 2, 1 SD), which is consistent with data reported by Selby and Creaser (2003) (0.10684 ± 0.00004). An in-house Re standard solution gave $^{185}Re/^{187}Re$ = 0.5937 ± 0.0016 (1 SD). The total procedural blanks for Os and Re were 0.06 pg and 2.4 pg, respectively, with an average $^{187}Os/^{188}Os$ value of 0.114 ± 0.004 ($n$ = 2).

For native gold samples <10 mg in weight, the total amount of Os liberated from the sample ranged from 0.05 to 3.80 pg, which in some cases was less than the analytical blank (0.06 pg). Therefore, the blank correction for these samples was significant, and the data are not reported with the final results. Only samples where blank constitutes less than 10% of total Os have been considered.

For the samples with sufficient sample material, Os model ages were estimated (Shirey and Walker, 1998). It is possible to estimate two different Os model ages: (Equation 1) $T_{MA}$, which is the time of separation from the chondritic mantle, which evolves according to the following equation:

$$T_{MA} = 1/\lambda \times \ln \{[(^{187}Os/^{188}Os_{PUM} - {}^{187}Os/^{188}Os_{sample}) / (^{187}Re/^{188}Os_{PUM} - {}^{187}Re/^{188}Os_{sample})] + 1\}$$

(Equation 1)

in which $\lambda$ is the $^{187}Re$ decay constant ($\lambda = 1.666 \pm 0.005 \times 10^{-11}$ $a^{-1}$), PUM is the elemental and isotope ratio for primitive upper mantle ($[^{187}Re/^{188}Os]_{PUM}$ = 0.4353 and $[^{187}Os/^{188}Os]_{PUM}$ = 0.1296); and (Equation 2) $T_{RD}$, which is the Re depletion model age, assuming a $^{187}Re/^{188}Os$ ratio = 0 at the time of formation:

$$T_{RD} = 1/\lambda \times \ln \{[(^{187}Os/^{188}Os_{PUM} - {}^{187}Os/^{188}Os_{sample}) / {}^{187}Re/^{188}Os_{PUM}] + 1\}$$

(Equation 2)

# Pb isotopes

Using the same digested material processed for Re–Os analysis, an aliquot was removed from the reverse aqua regia solution after Os extraction for Pb isotope analysis. Isolation of Pb from the matrix was achieved by passing the solution through AG1-X8 200–400 mesh anion exchange resin (Eichrom) in a HBr medium (Fig. 6). Final recovery of Pb from the column was achieved via 6N HCl.

In cases where galena inclusions were identified in the polished surfaces of some gold nuggets, a partial dissolution procedure modified from McNaughton et al. (1988) allowed selective 'etching' of galena inclusions within the insoluble gold. The section was first cleaned ultrasonically in water. After rinsing, a small drop of 3N HCl was placed over the galena inclusion for 5 minutes and rinsed off with water, and the process repeated. After these initial two-step etching, another small drop of 3N HCl was placed to cover the galena inclusion for 5 minutes and then recovered with a micropipette. The surface was rinsed again, and the process was repeated two times. The recovered Pb-bearing HCl solution from two-step leaching was dried down and redissolved in dilute nitric acid, ready for TIMS analysis.

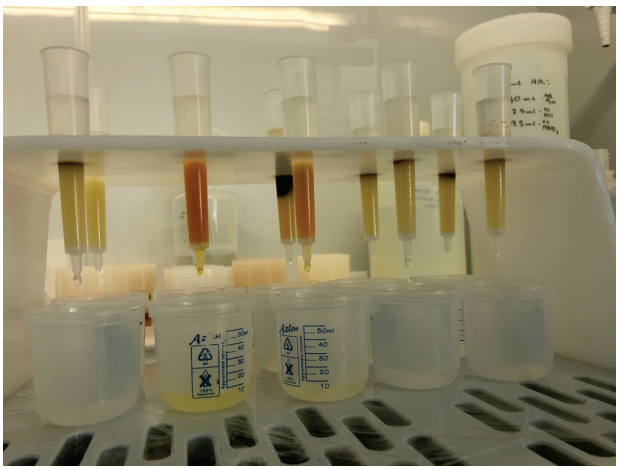

EAH179 28.03.22

Figure 6. Column chromatography setup for extraction of Pb from gold samples

Isotope ratios of Pb were measured using a ThermoFisher Triton mass spectrometer with Faraday cups in static mode. The sample–standard bracketing technique was used to externally correct fractionation bias for the majority of samples. Mass fractionation was estimated from the $^{207}Pb/^{204}Pb$ ratio of NBS-981 to be 0.02 per mil per mass unit. Procedural blanks were 0.23 ng Pb ($n$ = 2).

The double spike method was applied to selected samples with sufficient material. This method was set up within JdLC using the Southampton–Brest Pb $^{207}Pb–^{204}Pb$ (SBL74) double spike and protocols modified from Taylor et al. (2015). Ratios for each sample were measured in two different analytical sessions as a 'natural' session ('raw' sample loaded directly onto filament for analysis) and a double spiked session (a sample–spike mixture loaded together onto filament for analysis). Mass fractionation was corrected by calculation of the double spike and natural ratios using an iterative exponential law correction after the method of Woodhead et al. (1995) within a data reduction sheet provided by Professor Rex Taylor of the School of Ocean and Earth Science, in the National Oceanography Centre at the University of Southampton. For all sessions, the NIST SRM 981 Pb standard and an in-house 'Broken Hill' galena secondary RM were analysed for quality verification.

## Models of Pb evolution

Pb isotopes provide direct and indirect constraints on the age and tectonic environment of ores and their host rocks. Due to radioactive decay of $^{238}U$, $^{235}U$ and $^{232}Th$, the amounts of $^{206}Pb$, $^{207}Pb$ and $^{208}Pb$ respectively, increases with time. The rate of uranogenic Pb growth depends upon the original amount of Pb and the ratios between U and Pb, expressed as μ, which is defined as $^{238}U/^{204}Pb$. During formation of Pb-rich mineral deposits, Pb is extracted from source reservoirs and concentrated into Pb-rich, uranium-poor minerals, such as galena, pyrite and sphalerite (e.g. McNaughton et al., 1990).

In these minerals, radiogenic ingrowth of Pb ceases because U/Pb = ~0, preserving the initial ratios present in the source reservoir at the time of ore formation. However, trends to more radiogenic Pb compositions have been found within a single deposit, in a single hand specimen, and in centimetre-scale samples (McNaughton et al., 1990 and references therein). These more radiogenic compositions are attributed to either heterogeneous Pb at the time of mineralization, or to a younger resetting event (McNaughton et al., 1990). In the case of data trending toward more radiogenic Pb compositions, the least radiogenic end of the isotopic trend is considered to estimate the original Pb isotope composition at the time of ore formation for the studied deposit or sample. The initial ratios ($^{206}Pb/^{204}Pb$, $^{207}Pb/^{204}Pb$, $^{208}Pb/^{204}Pb$) of these minerals can be used to estimate the age of mineralization, if the Pb growth curve of the source region is established (e.g. Huston et al., 2014).

Although several global models of Pb isotope growth have been proposed (e.g. Stacey and Kramer, 1975; Cumming and Richards, 1975; Maltese and Mezger, 2020), they may have limited utility for age estimation in regional isotope reservoirs (although the Stacey and Kramers [1975] Pb evolution model has been used to construct a Pb isotope map of Australia; Huston et al., 2019). Two localized Pb isotope growth models have been established for Archean terranes in Western Australia: i) the Uchi–Wabigoon model (Thorpe et al., 1992), calibrated and most applicable to the Pilbara Craton, as well as some of the lode gold deposits in the Yilgarn Craton; ii) the Abitibi–Wawa model (Thorpe, 1999), which best applies to the Eastern Goldfields Superterrane of the Yilgarn Craton (Huston et al., 2014). Table 1 presents the parameters that define these models, predicting the age of many stratiform volcanic-hosted massive sulfide (VHMS) deposits in the local area to within 10 Ma of ages determined by independent methods such as zircon U–Pb. In addition to model ages, these Pb evolution models also produce μ values for the Pb source, which are used to compare deposits of disparate ages as the growth of radiogenic Pb is accounted for within this metric. Furthermore, the μ value is used to distinguish between juvenile (extracted from mantle) sources with low μ values, and evolved sources (with time-integrated 'crustal' signatures) with high μ values and more radiogenic Pb. Variations in μ values can be caused either by fractionation of U and Pb within the source region, or by mixing of two or more isotopically distinct sources (such as a juvenile mantle-derived source and an evolved source with a crustal signature).

## Platinum group elements

PGE concentrations were determined by isotope dilution. After the introduction of a tracer solution (containing Pt, Ir and Ru) and digestion, PGE were purified from the matrix solution during the same chromatography procedure used to extract Re. Once extraction was complete, the samples were redissolved and diluted in 1 ml of 0.8N $HNO_3$. Analyses of PGE were conducted as two separate groups (Group 1: Ru; and Group 2: Pt and Ir) within the same analytical session. Measurements of all masses of interest across the three methods were performed in low-resolution mode using electrostatic scanning (e-scan, i.e. peak jumping) from a set magnet mass. When in low-resolution mode of a magnetic sector-field ICP-MS, the large, flat peak tops and fast electronic scanning from a locked magnet position enable an improved measurement of the peak signal intensity via multiple sampling of peak tops. The analytical session was set up with a blank solution of 0.8N $HNO_3$ measured prior to the analysis of each unknown to correct for background. Operating parameters for the ICP-MS can be found in Table 2.

## Trace elements

The last aliquot of sample solution removed from the reverse aqua regia solution was used for trace element analysis and to perform quality checks on procedural and analytical processes. The aliquot was evaporated and redigested into 0.32N $HNO_3$ for ICP-MS analysis. Two different dilutions were made for trace element determination: a high-concentration solution was created for measurement of REE and a lower-concentration (more diluted) solution was created for measurement of high-concentration elements in Au (e.g. Ti, Cu, Zi, Pb, etc.). Trace element concentrations were acquired using a ThermoFisher HR-ICP-MS Element. After signal and instrument optimization was obtained using a 1 ng $g^{-1}$ tuning solution, measurements of trace elements and REE were performed in low resolution to obtain the highest sensitivity available due to the low REE contents of native gold. All elements were analysed in triple-counting mode to allow the determination of higher-concentration elements by analogue counting or on the Faraday detector at the same time as determining lower-concentration elements (e.g. REE) by pulse counting. Concentrations were determined via the relationship between the unknowns and a set of prepared standard solutions. Mixed standard solutions of different concentrations of the desired elements used for external concentration determinations were analysed after about every 10 unknowns. To monitor quality and potential memory effects, acid blanks were measured at regular intervals throughout the analytical sessions. To compensate for instrumental mass drift, the mass offset and automatic mass lock features of the ThermoFisher Element software were utilized in conjunction with each analytical blank being spiked with 1 ppb of In as an internal standard. An assessment of accuracy of the high-concentration elements in Au results was conducted using three RM for native Au. An assessment of accuracy of the REE results was not able

Table 1. Single-stage parameters employed for Pb isotope evolution models

| *Model* | *$T_0$ (Ma)* | *Initial ratios at $T_0$* | | | *$^{238}U/^{204}Pb$* | *Provinces* |
|---|---|---|---|---|---|---|
| | | *$^{206}Pb/^{204}Pb$* | *$^{207}Pb/^{204}Pb$* | *$^{208}Pb/^{204}Pb$* | | |
| Uchi–Wabigoon | 4 560 | 9.0818 | 9.9002 | 29.343 | 8.8 | Pilbara |
| Abitibi–Wawa | 4 490 | 9.4310 | 10.4950 | 29.681 | 8.0 | Kurnalpi |

**NOTES**: Parameters are from Thorpe et al. (1992), Thorpe (1999) and Huston et al. (2014)

to be properly conducted due to the lack of suitable RM for native Au. Operating parameters are presented in Table 2.

## Trace elements in gold reference materials

Three native gold RM (LBMA AuRM1, AuRM2 and AuRM3) were used for trace element analysis. All three RM have certified trace element data, which have been used to cross-check the quality of trace element analysis of unknown samples. For AuRM1 and AuRM2, 11 trace elements (out of 22 certified) were analysed at the JdLC (see Table 3). For AuRM3, seven elements (out of 12 certified) were analysed.

Chemical processing of RM was treated in a manner similar to the unknown natural gold samples (see Method section above). About 20 to 40 mg of gold was used for each dissolution and analysis. Each RM was analysed on three subsamples. Shavings were acid washed in 50% HCl, rinsed several times with distilled milli-Q water, and then dried in a clean fume hood. Samples were dissolved in a mixture of double-distilled acids (inverted aqua regia – hydrochloric and nitric acids in 1:3 ratio) at 60 °C for 60 hours. The resulting solutions were dried down and redissolved for trace element analysis using the same method described above for the unknowns (see 'Trace elements').

For AuRM1 and AuRM2, the majority of trace elements analysed agree with certified values within analytical precision (see Table 3, Fig. 7), with the exception of Bi (AuRM1 and AuRM2) and As (AuRM2). From these elements, Bi displays the most striking difference and requires more research. For AuRM3, all concentrations are below the certified values by around 80%, which could be related to incomplete dissolution of this RM.

As with the unknowns, the PGE concentrations were determined using the isotope dilution technique following the same procedure outlined above. For each RM, approximately 50 to 100 mg were digested with a PGE tracer solution and subsequently purified from the matrix solution via a chromatography procedure that extracts PGE into two groups (Group 1: Ru; and Group 2: Pt and Ir). After purification, RM were redissolved and diluted in 1 ml of 0.8N $HNO_3$ for analysis using the ThermoFisher HR-ICP-MS Element following the same analytical procedure as for the unknowns. Operating parameters for the ICP-MS are in Table 2. Background was removed and the tracer was stripped from the results offline. For our PGE results generated via the isotope dilution technique, the precision is about ten times better than certified (Fig. 8).

Table 2. Operating parameters for ThermoFisher Element XR sector-field HR-ICP-MS

| *Instrument settings* | | | | | |
|---|---|---|---|---|---|
| Sample gas (L/min) | 1.198 | | 1.217 | | |
| Auxilary gas (L/min) | 1.03 | | 1.03 | | |
| Cool gas (L/min) | 16.30 | | 16.32 | | |
| RF power (W) | 1300 | | 1300 | | |
| *Method settings* | *Rare earth elements* | *All other elements* | *Platinum group elements* | | |
| | | | *Ru* | *Pt, Ir* | *Pd* |
| Analysis time (s) | 41 | 43 | 81 | 91 | 112 |
| Runs/passes | 5/3 | 5/2 | 10/10 | 10/10 | 10/10 |
| Mass window | 20 | 20 | 10 | 10 | 10 |
| Integration window | 20 | 20 | 10 | 10 | 10 |
| Samples/peaks | 100 | 100 | 200 | 200 | 200 |
| Settling time (ms) | 1 | 1 | 1 | 1 | 1 |
| Deadtime (ns) | 13 | 13 | 13 | 13 | 13 |
| Mass resolution | Low | Low | Low | Low | Low |
| Sample time (ms) | 10 | 10 | 10 | 10 | 10 |
| Detection mode | Triple | Triple | Triple | Triple | Triple |

Table 3. Elemental concentrations in certified gold RM analysed at JdLC

| | *AuRM1* | | *AuRM2* | | *AuRM3* | |
|---|---|---|---|---|---|---|
| | *Certified* | *JdLC* | *Certified* | *JdLC* | *Certified* | *JdLC* |
| Ti | 10.5 ± 0.9 | 11.1 ± 1.6 | 31.6 ± 1.3 | 33.5 ± 4.3 | 7.8 ± 1.3 | 9.0 ± 0.7 |
| Mn | 9.7 ± 0.4 | 9.2 ± 1.7 | 28.2 ± 1.5 | 27.9 ± 4.1 | – | 0.2 ± 0.0 |
| Ni | 9.8 ± 1.0 | 9.5 ± 1.8 | 29.2 ± 2.6 | 29.3 ± 4.8 | 13.4 ± 1.0 | 14.7 ± 1.3 |
| Cu | 13.5 ± 2.7 | 13.4 ± 2.1 | 31.6 ± 2.4 | 34.1 ± 4.7 | 317 ± 11 | *360.5* ± 27.2 |
| Zn | 10.3 ± 1.2 | 10.6 ± 2.0 | 31.4 ± 2.3 | 31.8 ± 4.7 | 12.6 ± 1.5 | 14.2 ± 1.6 |
| As | 14.5 ± 1.0 | 14.9 ± 3.8 | 47.1 ± 2.8 | 35.0 ± 8.3 | – | 11.8 ± 4.1 |
| Pb | 9.8 ± 1.8 | 10.6 ± 0.4 | 28.9 ± 2.4 | 32.8 ± 2.6 | 23.6 ± 2.2 | 28.1 ± 1.6 |
| Pd | 9.7 ± 0.6 | 8.5 ± 1.5 | 29.2 ± 1.3 | 27.3 ± 4.4 | 25.8 ± 2.5 | 25.5 ± 2.1 |
| Pt* | 10.3 ± 1.1 | 9.6 ± 0.1 | 30.2 ± 2.1 | 27.1 ± 0.4 | 25.4 ± 1.6 | 24.0 ± 0.3 |
| Ru** | – | 1.9 ± 0.1 | – | 7.8 ± 0.2 | – | – |
| Ir** | – | 21.7 ± 0.7 | – | 20.1 ± 0.3 | 6300 ± 1800 | 4851 ± 57 |

**NOTES:** All measurements are in mg/kg. Uncertainties are standard deviations for three analysed subsamples (except for AuRM2 where only two subsamples were used). Values in *italics* are outside of reference values. Pt* and other PGE (except Pd) were analysed by the isotope dilution method similar to that applied for the 'unknown' native gold samples in this study (see 'Re-Os and PGE systematics' section). Ru** and Ir** (except for AuRM3) don't have certified values and were analysed for the first time. JdLC trace element results have less than 5% uncertainty

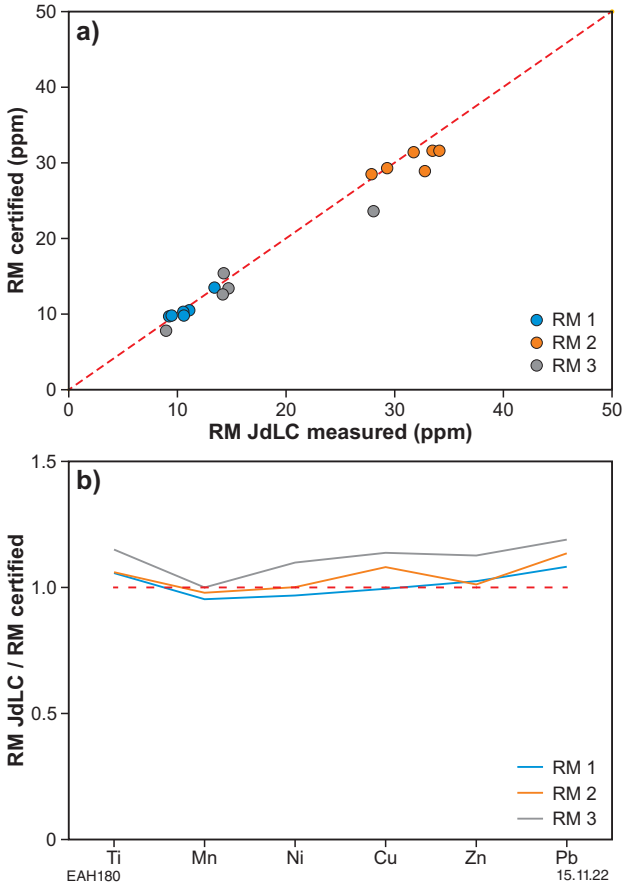


Figure 7. Trace element concentrations in certified RM AuRM1, AuRM2 and AuRM3: a) certified values vs values measured at JdLC – note that the majority of data fall on the 1:1 regression line; b) JdLC values normalized to certified concentrations

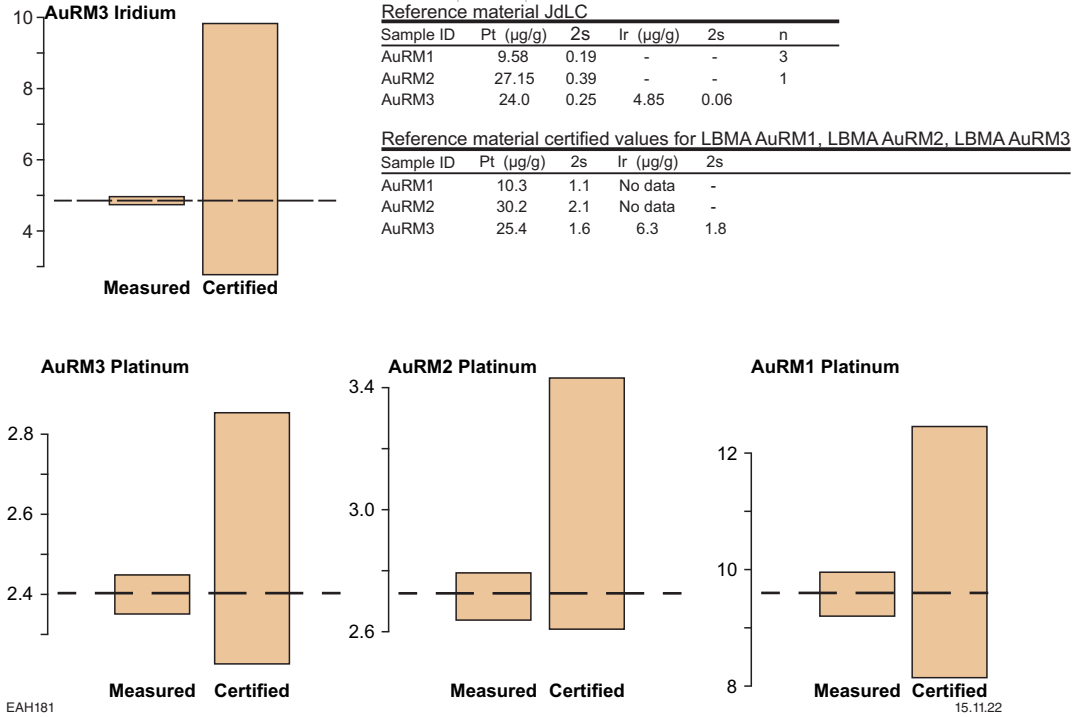


Reference material JdLC

| Sample ID | Pt (µg/g) | 2s | Ir (µg/g) | 2s | n |
|---|---|---|---|---|---|
| AuRM1 | 9.58 | 0.19 | - | - | 3 |
| AuRM2 | 27.15 | 0.39 | - | - | 1 |
| AuRM3 | 24.0 | 0.25 | 4.85 | 0.06 | |

Reference material certified values for LBMA AuRM1, LBMA AuRM2, LBMA AuRM3

| Sample ID | Pt (µg/g) | 2s | Ir (µg/g) | 2s |
|---|---|---|---|---|
| AuRM1 | 10.3 | 1.1 | No data | - |
| AuRM2 | 30.2 | 2.1 | No data | - |
| AuRM3 | 25.4 | 1.6 | 6.3 | 1.8 |

Figure 8. Platinum (from all three RM) and iridium (from AuRM3) concentrations measured at JdLC compared to certified values. Note that measurements using isotope dilution at JdLC are an order of magnitude more precise than certified values

# Kurnalpi goldfield, Yilgarn Craton

## Geological setting

The Kurnalpi goldfield is located about 85 km east-northeast of Kalgoorlie in the Kurnalpi Terrane of the Eastern Goldfields Superterrane in the Yilgarn Craton (Hancock and Beardsmore, 2020). Local bedrock consists of 2960– 2650 Ma metamorphosed basalt (GSWA, 2020), with zones of dolerite and feldspar–hornblende or chlorite schist. Known sub-economic bedrock-hosted gold mineralization in the area appears to have been orogenic style that are documented in greenstone belts throughout the Yilgarn Craton (e.g. Groves et al., 1998). The mineralization occurs in quartz veins with microscopic gold and associated silica–pyrite±carbonate±hematite alteration in metabasalt, and in magnetite-bearing, granophyric quartz dolerite dykes that cut ultramafic rocks.

This study uses nine placer gold nuggets sourced from six widely distributed sites over an area of 40 km$^2$ (Fig. 9). The nuggets were collected from thin gravels at the base of Quaternary channels buried 1–2 m beneath surficial loam, from Cenozoic laterite and calcrete deposits, and from buried paleochannels (Schupp, 1985). There are up to 40 m of detrital zones in the Cenozoic regolith that preserve the history of weathering, erosion and landscape development (Schupp, 1985). In addition, the Yilgarn Craton was extensively glaciated during the early Permian and was at least locally incised by subglacial channels (Eyles and de Broekert, 2001).

## Pb–Pb isotope systematics

Six gold nuggets, including two with galena inclusions, were analysed for Pb isotopes (Table 4 and Appendix 2). The least radiogenic data indicate Archean model ages, and are compared to data for c. 2.7 Ga VHMS ores in the Kurnalpi Terrane (Fig. 10a). The VHMS comparison demonstrates that initial Pb in the terrane was variable, and different nuggets may have different sources and hence not have had the same initial Pb at the time of formation. A 2.7 Ga isochron (approximate model age for galena) fitted to the galena data is shown for reference.

Galena inclusions yield the most primitive Pb isotope compositions, with $^{206}Pb/^{204}Pb$ ratios of 13.53 and 13.55 (Table 4, Fig. 10a) and Neoarchean model ages of 2.66 and 2.65 Ga (Abitibi–Wawa model; Thorpe, 1999) or 2.72 and 2.71 (Uchi–Wabigoon model; Thorpe et al., 1992). These model ages are similar to the Re–Os molybdenite age of 2661 ± 10 Ma from gold-bearing cross-cutting silica–carbonate lodes at the Wallaby gold deposit (Mueller et al., 2008) and Syenitic Group intrusions in the Kurnalpi Terrane (2.66 Ga; Witt et al., 2018, and references therein).

Pb isotopes in the gold nuggets are slightly more radiogenic than those for the galena inclusions that were extracted from them. For example, native gold from GSWA 201943 is 0.4 to 0.6% more radiogenic than galena inclusions in the same nugget ($^{206}Pb/^{204}Pb$ ratios are 13.59 and 13.61 for two analyses). Sample GSWA 201954, which contains no visible galena inclusions, also indicates a more radiogenic $^{206}Pb/^{204}Pb$ ratio of 13.82 and a younger Pb model age of 2.44 Ga.

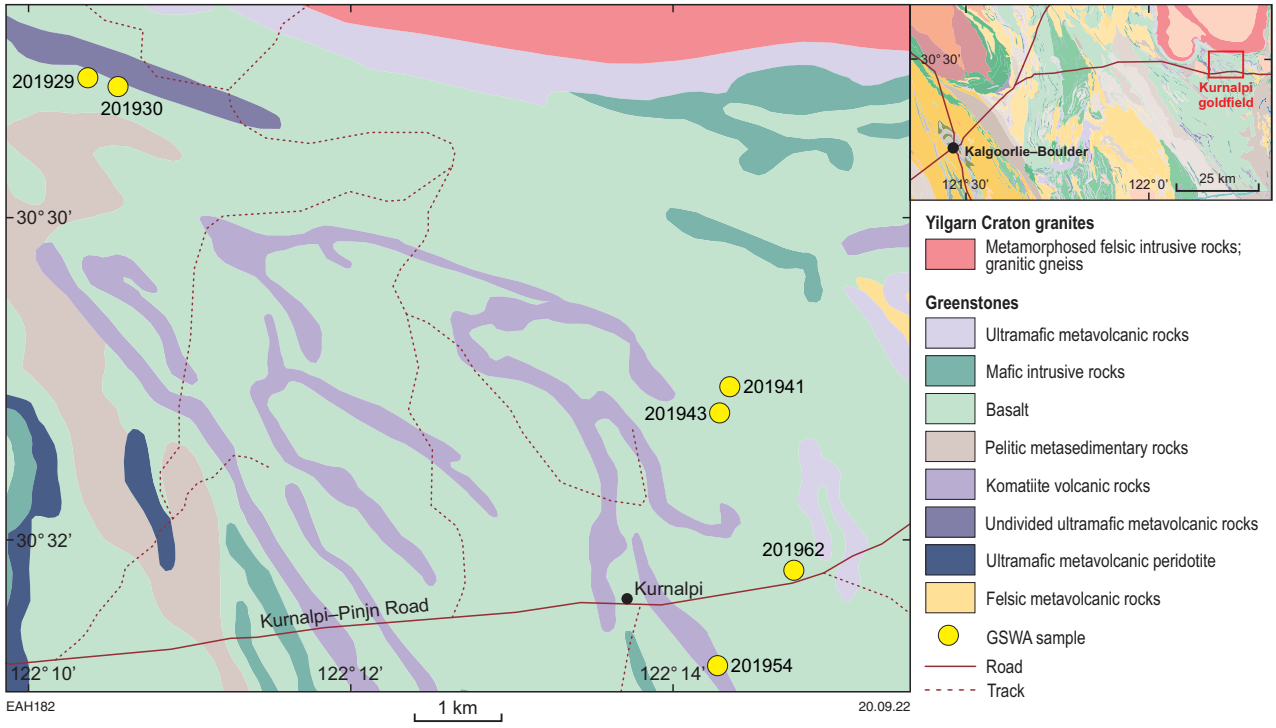


Figure 9. Geological map of Kurnalpi goldfield and locations of samples. Bedrock geology from GSWA (2020)

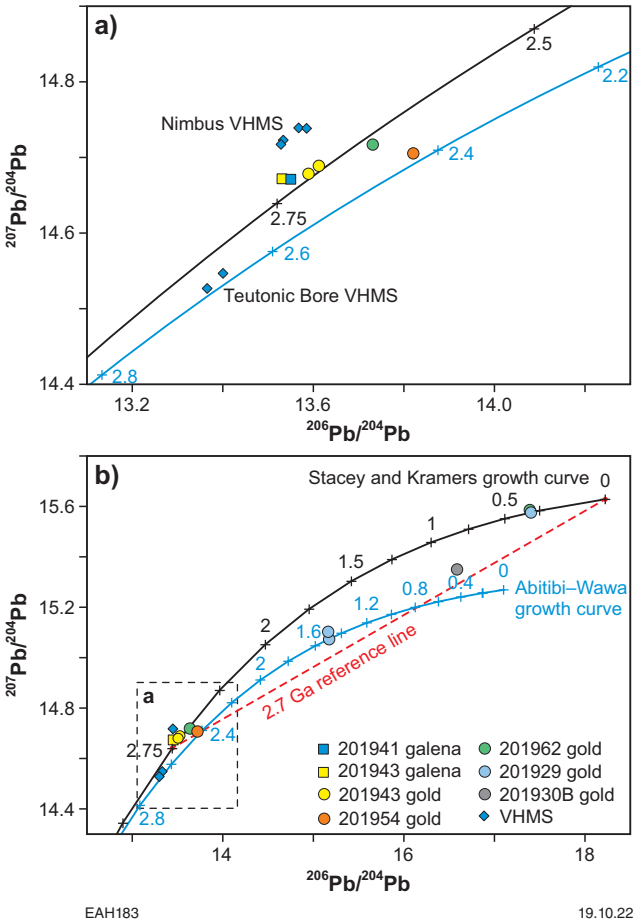


Figure 10. Plot of $^{207}Pb/^{204}Pb$ vs $^{206}Pb/^{204}Pb$ for samples from the Kurnalpi Terrane: a) the Pb isotope compositions of galena from c. 2.7 Ga stratiform VHMS deposits at Teutonic Bore and Nimbus are shown for comparison (data from Browning et al., 1987; Barrote et al., 2020a,b); b) the Pb isotope compositions of gold and galena from Kurnalpi goldfield

Table 4. Pb isotope compositions and source μ-values ($^{238}U/^{204}Pb$) for Kurnalpi goldfield samples

| Sample ID | Material analysed | $^{206}Pb/^{204}Pb$ | $^{207}Pb/^{204}Pb$ | $^{208}Pb/^{204}Pb$ | $Age_1$ (Ga) | $^{238}U/^{204}Pb_1$ | $Age_2$ (Ga) | $^{238}U/^{204}Pb_2$ |
|---|---|---|---|---|---|---|---|---|
| 201929A | Gold | 17.813 ± 23 | 15.575 ± 27 | 37.875 ± 54 | 0.15 | 8.53 | 0.32 | 8.9 |
| 201929A-R | Gold | 15.386 ± 32 | 15.101 ± 30 | 35.201 ± 69 | 1.53 | 8.06 | 1.65 | 8.5 |
| 201929B | Gold | 15.398 ± 74 | 15.072 ± 81 | 35.406 ± 206 | 1.49 | 7.99 | 1.61 | 8.5 |
| 201930B | Gold | 16.928 ± 82 | 15.349 ± 95 | 37.291 ± 204 | 0.58 | 8.21 | 0.73 | 8.6 |
| 201941 | Galena | 13.551 ± 1 | 14.671 ± 1 | 33.317 ± 1 | 2.65 | 8.25 | 2.71 | 8.8 |
| 201943 | Galena | 13.532 ± 2 | 14.671 ± 2 | 33.383 ± 7 | 2.66 | 8.28 | 2.72 | 8.9 |
| 201943 | Gold | 13.613 ± 13 | 14.688 ± 15 | 33.404 ± 31 | 2.61 | 8.24 | 2.67 | 8.8 |
| 201943-R | Gold | 13.590 ± 4 | 14.678 ± 4 | 33.367 ± 10 | 2.62 | 8.23 | 2.68 | 8.8 |
| 201954 | Gold | 13.822 ± 3 | 14.705 ± 3 | 33.574 ± 7 | 2.44 | 8.04 | 2.71 | 8.82 |
| 201962B | Gold | 17.798 ± 4 | 15.585 ± 5 | 37.696 ± 12 | 0.18 | 8.55 | 0.34 | 8.9 |
| 201962B-R | Gold | 13.732 ± 3 | 14.717 ± 4 | 33.545 ± 9 | 2.53 | 8.17 | 2.60 | 8.7 |

**NOTES:** -R suffix on the sample ID indicates a repeat analysis of the same sample. $Age_1$ and $(^{238}U/^{204}Pb)_1$ were calculated using the Abitibi–Wawa model (Thorpe, 1999). $Age_2$ and $(^{238}U/^{204}Pb)_2$ were calculated using the Uchi–Wabigoon model (Thorpe et al., 1992). Analytical uncertainty is standard deviation (SD)

For some samples, replicate analyses yielded variable results (Table 4). Gold nugget GSWA 201962B contains small Ag–Au telluride inclusions and displays variable Ag, Cu and Hg contents in its recrystallized phases (Appendix 1). Subsample GSWA 201962B-R, drilled out of the original nugget, has a relatively unradiogenic Pb isotope composition, with $^{206}Pb/^{204}Pb$ = 13.732, whereas subsample GSWA 201962B, which was scratched from the polished surface of the resin-mounted nugget, indicates a more radiogenic Pb isotope composition, with $^{206}Pb/^{204}Pb$ = 17.798. The single-stage model age of this radiogenic Pb varies, depending on the model chosen, from 0.18 to 0.34 Ga (Table 4), or 0.59 Ga according to the Stacey and Kramers (1975) two-stage model. Variations in the more radiogenic data are probably attributable to mixing of material from the nugget core, which preserves a primitive Neoarchean Pb signature, with material in marginal recrystallized zones, which exhibits modified Pb signatures due to in situ U decay and/or younger alteration.

Similarly, GSWA 201929 consists of two separate gold nuggets (A and B), which were analysed separately. Nugget GSWA 201929A was analysed twice and also displays heterogeneous Pb isotope compositions, similar to GSWA 201962B. Subsample GSWA 201929A (scratched from the surface) displays the most radiogenic $^{206}Pb/^{204}Pb$ of 17.813; whereas repeated drilled subsample 201929A-R yields a less radiogenic isotope composition with $^{206}Pb/^{204}Pb$ of 15.386. Model ages for the most radiogenic sample vary greatly depending on the model used, from 0.32 to 0.15 Ga (Table 4), or 0.56 Ga according to the Stacey and Kramers (1975) model. The least radiogenic repeat analysis corresponds to much older model ages of 1.53 to 1.65 Ga (Table 4). This well-rounded nugget contains inclusions of maghemite and has a relatively high Cu content (430–546 ppm), which is interpreted to indicate a distal provenance with a Cu-rich source. The chemically stable maghemite is formed by oxidation of magnetite during some weathering processes, including near-surface heating, such as bushfires (Hancock and Beardsmore, 2020).

Nugget GSWA 201929B has a Pb isotope composition similar to that of GSWA 201929A-R with $^{206}Pb/^{204}Pb$ of 15.398. This data plots in an intermediate position between the most primitive Neoarchean cluster and more radiogenic Pb values (Fig. 10b). This sample is heterogeneous and contains Cu-depleted zones, spikes in Hg and Sb, and small Ag–Au telluride inclusions (Appendix 1).

Sample GSWA 201930B has a $^{206}Pb/^{204}Pb$ ratio of 16.928 and plots below the Stacey and Kramers growth curve but above the Abitibi–Wawa Pb growth curve (Fig. 10b). This well-rounded ferruginous nugget is representative of other rounded nuggets in the Kurnalpi goldfield in terms of chemical composition and simple microstructure with only marginal alteration (Appendix 1).

All of the more radiogenic Pb isotope data fall above the 2.7 Ga reference line (Fig. 10b). The position of the more radiogenic compositions could reflect an Archean nugget and either in situ U decay from an initial Pb more radiogenic (in $^{207}Pb/^{204}Pb$) than the galena data, and/or a more complex history, particularly at younger times.

A weak correlation exists between the Pb isotope composition and trace elements such as Cu (Fig. 11), indicating that the most radiogenic Pb data may correspond to samples with elevated Cu contents. Thus, these trace elements may indicate the degree of alteration of the samples.

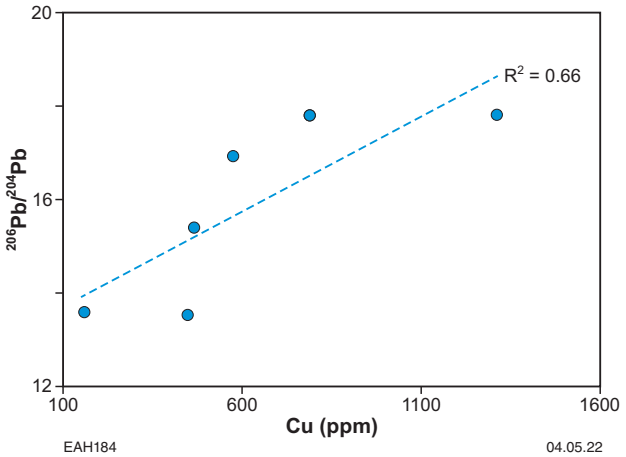


Figure 11. Plot of $^{206}Pb/^{204}Pb$ vs Cu contents in samples from the Kurnalpi goldfield. $R^2$ = correlation coefficient

## Source of Pb

The source of metals (including gold) in epithermal and orogenic gold deposits has been considered mainly as crustal, based on lithophile element isotope systematics (Sr–Pb–Nd–Hf) (e.g. Kerrich et al., 1987; McNaughton et al., 1990; Mueller et al., 1991). To investigate the sources of Pb in native gold, we refer to the better-known stratiform VHMS deposits from the same area, formed around 2.7 Ga (e.g. Barrote et al., 2020a). The initial Pb for two VHMS deposits (Teutonic Bore and Nimbus) are shown in Figure 10a. The Teutonic Bore deposit belongs to the Teutonic Bore camp located within the Kurnalpi Terrane and is the most relevant to this study (e.g. Barrote et al., 2020b). The Nimbus VHMS deposit is situated near the boundary between the Kalgoorlie and Kurnalpi Terranes (Barrote et al., 2020a).

The Teutonic Bore deposit displays the most primitive Pb isotope composition with the most primitive model source μ-value ($^{238}U/^{204}Pb$) of 8.1 (recalculated after McNaughton et al., 1990; Fig. 12). This low μ-value is consistent with S isotope composition of ore sulfides being mainly of mantle origin ($\delta^{34}S$ = −0.83 to +1.89‰; $\Delta^{33}S$ = −0.46 to −0.05‰) and distinct from sedimentary sulfides ($\delta^{34}S$ = +0.88 to +14.86‰; $\Delta^{33}S$ = +0.19 to +6.20‰) both locally and regionally (Chen et al., 2015). Chen et al. (2015) suggested the mantle S was likely derived from a magmatic–hydrothermal fluid, rather than by leaching from magmatic sulfides in the footwall volcanic rocks.

The Nimbus deposit displays a higher source μ-value of 8.4 (recalculated after Barrote et al., 2020a; Fig. 12). High-grade Zn–Ag mineralization at the Nimbus deposit was interpreted as having a mainly magmatic sulfur source (Caruso et al., 2018), based on sulfur isotope signatures suggestive of sulfur and fluids being sourcing largely from a magmatic reservoir ($\Delta^{33}S$ = +0.09‰).

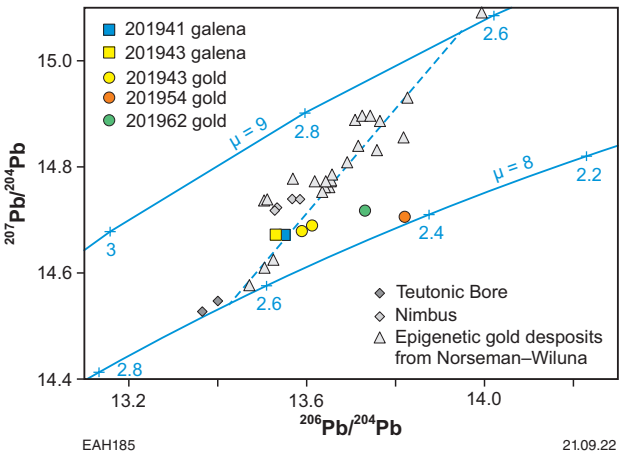


Figure 12. Plot of $^{207}Pb/^{204}Pb$ vs $^{206}Pb/^{204}Pb$ for samples from the Kurnalpi goldfield compared to data for stratiform VHMS deposits (Nimbus and Teutonic Bore) and epigenetic gold mineralization from the Norseman–Wiluna Terrane (data from McNaughton et al., 1990 and Barrote et al., 2020a,b). Lead growth curves for two different μ values ($^{238}U/^{204}Pb$) are shown. Data are distributed along the line depicting similar age but different μ values, interpreted to reflect mixtures between more juvenile (e.g. Teutonic Bore) and more 'crustal' sources

The μ value for galena inclusions in native gold and the less radiogenic gold nuggets from Kurnalpi plots between those for the Teutonic Bore and Nimbus deposits (Fig. 12), which may suggest a juvenile, predominantly mantle, source of Neoarchean age. Note that the age of gold mineralization in the Eastern Goldfields is about 2.64 Ga (Vielreicher et al., 2015), and the less radiogenic Pb data from native gold is compatible with these deposits.

# Re–Os systematics

The Re and Os elemental and isotope compositions were measured in selected samples (Table 5). The Os contents vary from 0.2 to 687 ppt, with a median of 47 ppt. The median Os contents of the gold are similar to that of the average continental crust (31 ppt, Rudnick and Gao, 2003). These values are also similar to polymetallic ores from the Nimbus VHMS deposit, which vary from 7 to 78 ppt, and are lower than those in pyrite from the same deposit (119–757 ppt; Barrote et al., 2020a).

The Re values are between 1 and 37 ppb, with a median of 10 ppb. These values are similar to or higher than average continental crust (different estimates vary between 0.2 to 2 ppb) (Esser and Turekian, 1993; Sun et al., 2003), and similar to or higher than Re contents in sulfide ores from the Nimbus VHMS deposit (0.4 – 17.6 ppb; Barrote et al., 2020a). There is a correlation ($R^2$ = 0.92) between Re and Os contents (Fig. 13) and between Re/Os and Zn for six samples.

Studies of Re and Os in native gold are scarce. Gold from the Witwatersrand province in South Africa (Kirk et al., 2002) has Os contents 3 to 6 orders of magnitude higher (4 to 73 ppb, with one data point at 4 ppm; Fig. 14). The study by Kirk et al. (2002) used significantly higher sample weights and this discrepancy highlights the potential of the 'nugget effect' with possible Os-bearing nugget inclusions dominating the Os budget in Witwatersrand gold. Another study of Re–Os systematics in native gold from the Grasberg gold deposit in Papua provided only one analysis of gold, which yielded higher Os (873 ppt) and lower Re (0.6 ppb) contents, compared to the Kurnalpi nuggets.

Most Kurnalpi samples have unradiogenic Os isotope compositions, with $^{187}Os/^{188}Os$ of 0.12 to 0.29. Least radiogenic values are close to those for Archean mantle (present mantle $^{187}Os/^{188}Os$ = 0.127; Shirey and Walker, 1998). This is surprising given that the radioactive decay of Re since the Archean should produce more highly radiogenic $^{187}Os/^{188}Os$ ratios due to radiogenic $^{187}Os$ isotope ingrowth. For example, the lowest $^{187}Os/^{188}Os$ ratio for pyrite from the Nimbus VHMS deposit is 17.9, increasing to 58.0 (as measured today). The least radiogenic $^{187}Os/^{188}Os$ ratio of 0.50 from the Nimbus deposit was recorded in polymetallic second-stage ore (Barrote et al., 2020a). These polymetallic ores bear some similarities in terms of Re–Os elemental and isotope composition with the Kurnalpi nuggets.

Sample GSWA 201943 has the lowest concentration of Os (0.2 ppt), which is close to the blank values, and also displays an unradiogenic Os composition of 0.115, which corresponds to the Archean mantle value (ca. 2 Ga; see Shirey and Walker, 1998 for calculations). A repeat analysis of the same sample with a larger sample amount produced higher Os contents of 5 ppt, but a similar unradiogenic ratio of 0.119.

Table 5. Re and Os elemental and isotope compositions of Kurnalpi goldfield samples

| *Sample ID* | *Re (ppb)* | *Os (ppt)* | *$^{187}Re/^{188}Os$* | *$^{187}Os/^{188}Os$* | *$T_{MA}$ (Ma)* |
|---|---|---|---|---|---|
| 201929B | 11.85 ± 0.40 | 32.6 ± 1.1 | 713 ± 24 | 0.2936 ± 0.0126 | – |
| 201929A-R | 1.45 ± 0.11 | 2.4 ± 0.05 | 1117 ± 175 | 0.1870 ± 0.0171 | – |
| 201930B | 24.19 ± 1.50 | 69.4 ± 0.76 | 912 ± 53 | 0.1911 ± 0.0066 | – |
| 201943 | – | 0.21 ± 0.02 | – | 0.1151 ± 0.0016 | – |
| 201943-R1 | 7.18 ± 0.16 | 5.4 ± 0.19 | 2302 ± 85 | 0.1197 ± 0.0122 | |
| 201954 | 1.20 ± 0.02 | 13.6 ± 0.48 | 903 ± 39.3 | 8.7302 ± 0.3546 | 570 |
| 201962A | 37.12 ± 1.40 | 687.3 ± 2.0 | 235 ± 11 | 0.1271 ± 0.0005 | – |
| 201962B-R | 7.65 ± 0.31 | 8.0 ± 0.1 | 2965 ± 121 | 0.1317 ± 0.005 | – |

**NOTES:** -R suffix on the sample ID indicates a repeat analysis of the same sample. $T_{MA}$ refers to the age of separation from mantle (see Methods section for details). Analytical uncertainty is 2 sigma

Because the same sample yields a primitive Pb isotope composition and a Neoarchean model age, it is likely that the native gold at the Archean time was virtually free of Re. The preserved Os isotope composition suggests a mantle origin for Os.

Most Kurnalpi samples display similarly low unradiogenic $^{187}Os/^{188}Os$ ratios ranging from 0.115 to 0.29. Preservation of such low $^{187}Os/^{188}Os$ ratios would require a very low mantle-like Re/Os ratio (<1) within a sample (i.e. red line in Fig. 15). Paradoxically, the measured Re/Os ratios of these samples are higher, which could be explained by either much later Re addition, and/or the low sample weight of gold analysed, compared to the analytical blank. In the former case, Os would reside in gold in the form of Os-rich alloys with minimal (close to zero) Re contents. If the Re was added at a later time, the Re would be decoupled from Os and thus account for unradiogenic Os, yet a high Re/Os ratio. In the latter case, the (relatively) high Re contents may be an analytical artefact and future studies should use larger sample sizes to minimize the relative blank contribution.

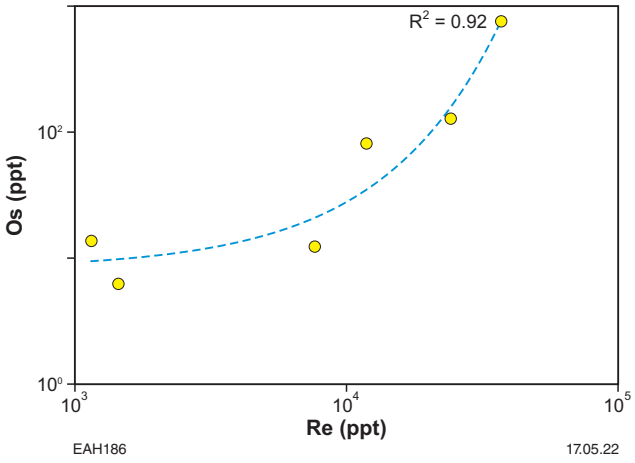


Figure 13. Os vs Re concentrations for samples from the Kurnalpi goldfield. The correlation coefficient ($R^2$) of 0.92 is significant

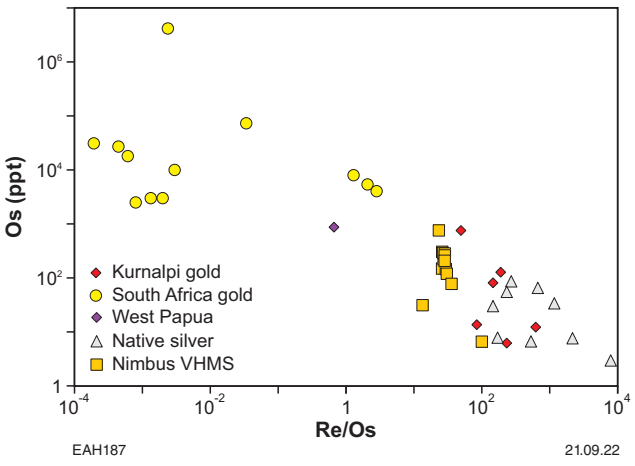


Figure 14. Os concentration vs Re/Os ratio for samples from the Kurnalpi goldfield compared to data from South Africa (Kirk et al., 2002), West Papua (Mathur et al., 2005), GSWA unpublished data on native silver, and the Nimbus VHMS deposit (Barrote et al., 2020a)

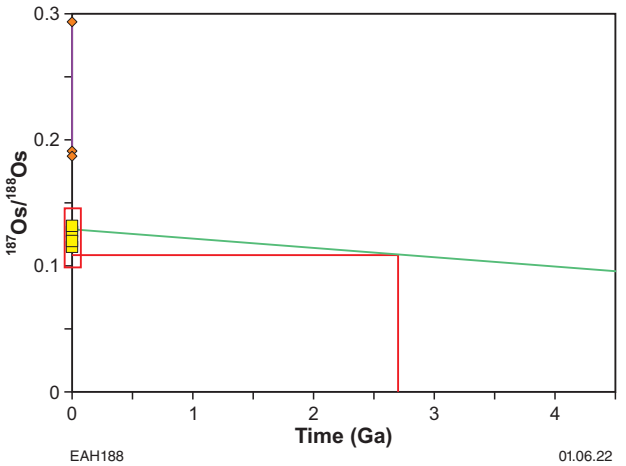


Figure 15. Plot of $^{187}Os/^{188}Os$ for samples from the Kurnalpi goldfield relative to the Os mantle evolution curve (green). Samples with unradiogenic Pb compositions are shown as yellow squares. The Os ratios for mantle evolution are taken from Shirey and Walker (1998)

GSWA 201954 is the largest sample analysed (0.3 g) and produced the most radiogenic $^{187}Os/^{188}Os$ ratio from this study of 8.73 (Table 5 and Fig. 16). Its Re–Os model age is 570 Ma (using initial $^{187}Os/^{188}Os$ = 0.12 – present mantle). This model age represents a maximum estimate and could be younger if the initial $^{187}Os/^{188}Os$ is higher than the assumed mantle value.

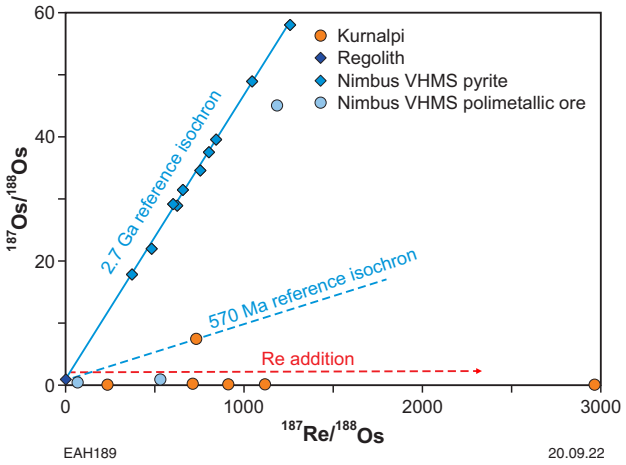


Figure 16. Re–Os isochron diagram for samples from the Kurnalpi Terrane. Data for colloform pyrite and polymetallic ore from the Nimbus VHMS deposit are shown for comparison (Barrote et al., 2020a) to define the expected ~2.7 Ga reference isochron. Note that the most radiogenic sample (GSWA 201954) plots off the 2.7 Ga reference isochron and has an apparent age of 570 Ma (using initial $^{187}Os/^{188}Os$ = 0.12)

## Platinum group element studies

Data for PGE concentrations are presented in Table 6 and plotted in Figure 17. Native gold samples from the Kurnalpi Terrane contain 1.7 to 56.8 ppb Pt, 0.2 to 0.4 ppb Ru, 0.04 to 1.28 ppb Ir, and 0.10 to 1.61 ppb Pd (Table 6) and show distinct enrichment in Pt and Pd (P-PGE: Rh, Pt, Pd) over Ir, Os and Ru (I-PGE: Os, Ir, Ru), with Pd/Os >> 1.

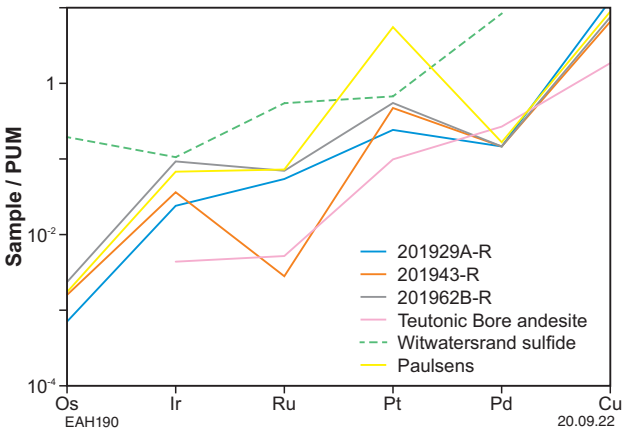


Figure 17. Primitive mantle-normalized PGE and Cu patterns for samples from the Kurnalpi goldfield, compared to Teutonic Bore andesite (Park and Campbell, 2020), Witwatersrand sulfides (Schaefer et al., 2010) and Paulsens gold deposit (this Report)

Table 6. PGE compositions of samples from the Kurnalpi goldfield

| *Sample ID* | *Ir* | *2σ* | *Ru* | *2σ* | *Pt* | *2σ* | *Pd* | *2σ* |
|---|---|---|---|---|---|---|---|---|
| 201929A | – | | 0.26 | 0.10 | – | | 0.16 | – |
| 201929B | 1.28 | 0.23 | 0.27 | 0.18 | 50.90 | 0.96 | 0.58 | 0.03 |
| 201929A-R | 0.08 | 0.01 | 0.27 | 0.02 | 1.71 | 0.15 | 0.57 | 0.03 |
| 201930A | 0.04 | 0.26 | 0.40 | 0.10 | 56.83 | 1.38 | 0.16 | 0.01 |
| 201930B | 0.03 | 0.02 | 0.26 | 0.10 | 53.36 | 0.92 | 0.59 | 0.03 |
| 201930C | 0.13 | 0.05 | 0.20 | 0.06 | 46.78 | 1.16 | 0.13 | 0.01 |
| 201943 | 0.09 | 0.05 | 0.31 | 0.10 | 21.41 | 0.61 | 0.41 | 0.02 |
| 201943-R | 0.12 | 0.03 | 0.01 | 0.00 | 3.34 | 0.38 | 0.57 | 0.03 |
| 201943-R1 | – | | 0.19 | 0.06 | 29.50 | 1.03 | 0.10 | 0.01 |
| 201962A | – | | 0.34 | 0.12 | – | | 0.20 | 0.01 |
| 201962B | 0.66 | 4.61 | – | | 47.58 | 2.30 | 1.61 | 0.08 |
| 201962A-R | 0.30 | 0.04 | 0.35 | 0.02 | 3.89 | 0.65 | 0.57 | 0.03 |

**NOTES:** -R suffix on the sample ID indicates a repeat analysis of the same sample; all measurements are in ppb.
Analytical uncertainty is 2 sigma

The overall pattern of PGE distribution is similar to that of andesites from the Teutonic Bore complex of the Kurnalpi Terrane (Park and Campbell, 2020). Similarity between PGE patterns for volcanic rocks from the Kurnalpi Terrane (Park and Campbell, 2020) and that of native gold, together with mantle-like Os signatures, suggests that the PGE may come from a PGE-bearing magmatic–hydrothermal fluid exsolved from an underlying magma chamber, or from a fluid released during metamorphism of, or fluid interaction with, host volcanic rocks, preserving the initial PGE signature. The PGE contents in Kurnalpi samples are lower than that for the representative sulfide sample from the Witwatersrand province in South Africa (Schaefer et al., 2010).

## Trace elements

Trace element abundances are summarized in Appendix 3 and shown on Figure 18; correlation coefficients are tabulated in Table 7. Note that correlation coefficients are notional, given the number of analyses is <30, which is considered the minimum number for reliable statistical assessments.

In the analyzed solutions of Kurnalpi gold nuggets, median trace element abundances decrease in the following order (in ppm): Cu [623] → As [54] → Zn [18] → V [15] → Ti [8] → Ni [2] → Pb [2] Mn [0.5] → Co [0.1] → Cd [0.1] → Bi [0.04] → U [0.006]. The maximum Cu, Zn and Pb abundances occur in sample 201962A, likely due to inclusions within the gold. Repeated analysis of the same sample with a larger amount of material returned much lower concentrations of these elements, close to those determined by LA-ICP-MS (Hancock and Beardsmore, 2020). Sample GSWA 201929A returned high Cu contents (1312 and 1900 ppm) in both the primary analysis and duplicate. This well-rounded gold nugget with marginal recrystallization also returned the highest Cu contents by LA-ICP-MS (430–546 ppm) and was interpreted as having originated from a distal Cu-rich source. In addition to the highest Cu contents of the sample suite, GSWA 201929A has the most radiogenic Pb ratios (Fig. 11). The samples with highest Cu and Zn contents also have the highest Pd, Ni and Pb contents, which suggests an association between these elements (Table 7). The correlation coefficients calculated for Cu decrease in the following order: Cu → Pd → Zn → Pb → Pt (0.90 → 0.86 → 0.85 → 0.65 correspondingly). For Pb, a similar range has been calculated: Pb → Zn → Ni → Pd → Cu (0.99 → 0.93 → 0.90 → 0.85 correspondingly).

## Rare earth elements

The REE data (Table 8) and distribution patterns are shown in Figure 19. The overall slope and REE contents are similar to or lower than those for ore-hosting andesite from the Kurnalpi Terrane (Park and Campbell, 2020). The enrichment in light REE is pronounced, with a slight Ce anomaly present in some samples.

# Paulsens and Mount Olympus gold deposits, Capricorn Orogen

## Geological setting

The Paulsens and Mount Olympus gold deposits are located in the northern part of the Proterozoic Capricorn Orogen (Fig. 20), close to splays associated with the Nanjilgardy Fault system, a major mantle-tapping structure formed along the southern margin of the exposed Pilbara Craton (Hancock and Thorne, 2016; Fielding et al., 2017).

The Paulsens orogenic gold deposit is located in the northwestern Wyloo Dome, which formed during the 2215–2145 Ma Ophthalmian Orogeny and was subsequently reactivated during the 1820–1770 Ma Capricorn Orogeny (Sheppard et al., 2005). Gold mineralization occurs in a structurally controlled, 40 m-thick quartz vein, hosted by low-grade metasedimentary and metavolcanic rocks of the 2775–2629 Ma Fortescue Group. Fielding et al. (2017) reported two gold mineralization events at Paulsens, at c. 2400 and 1680 Ma.

The Mount Olympus sedimentary-hosted gold deposit lies in the Ashburton Basin, southeast of the Bellary Dome near Paraburdoo. Mineralization (1738 Ma; Sener et al., 2005) comprises submicroscopic gold inclusions in disseminated arsenian pyrite, associated with quartz–sericite alteration in Paleoproterozoic rocks of the Wyloo Group. Gold nuggets were collected 2–3 km away from the main deposit in quartz-rich colluvium overlying faulted Beasley River Quartzite and Cheela Springs Basalts. The nuggets are interpreted to have formed during the final stages of c. 1738 Ma dextral strike-slip faulting in the southern Pilbara, or during one of the many Paleoproterozoic to Neoproterozoic tectonic events recorded in the central Capricorn Orogen (Hancock and Thorne, 2016).

## Pb–Pb isotope systematics

Three gold samples from the Paulsens and Mount Olympus gold deposits (Fig. 1 and Appendix 1) were analysed (Table 9). Primary ore from the Paulsens orogenic gold deposit (rock chip GSWA 201909) was obtained from a stylolitic quartz vein at the Voyager 1 Upper Zone, and yields a $^{206}Pb/^{204}Pb$ ratio of 15.533. Gold nuggets GSWA 201912 and GSWA 201914C were obtained from quartz-rich colluvium proximal to the Mount Olympus main sedimentary-hosted gold deposit. A gold nugget intergrown with vein quartz (GSWA 201912) was analysed twice, yielding $^{206}Pb/^{204}Pb$ ratios of 16.68 and 17.84. Free gold nugget GSWA 201914C displays the most primitive Pb isotope composition, with a model age of 1.66 Ga (Cumming and Richards, 1975).

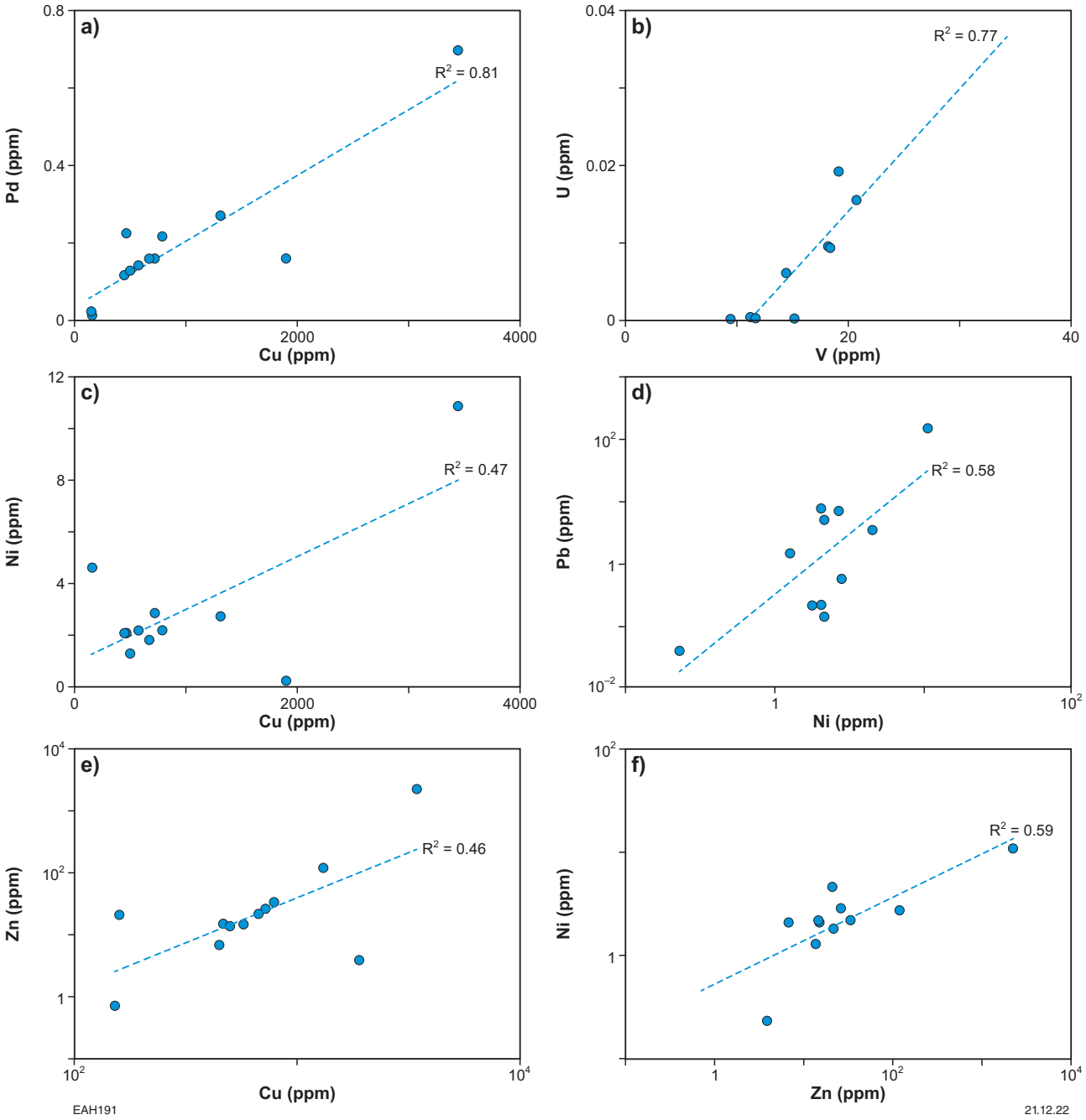


Figure 18. Trace element concentrations for samples from the Kurnalpi goldfield (Table 7). $R^2$ = correlation coefficient

Table 7. Correlation coefficients between trace elements (including PGE and some REE) for samples from the Kurnalpi goldfield

| | *Ti* | *V* | *Mn* | *Co* | *Ni* | *Cu* | *Zn* | *As* | *Yt* | *Cd* | *Pb* | *Bi* | *U* | *Pt* | *Ru* | *Ir* | *Pd* | *La* | *Lu* |
|---|---|---|---|---|---|---|---|---|---|---|---|---|---|---|---|---|---|---|---|
| *Ti* | 1 | 0.38 | 0.34 | -0.17 | 0.00 | 0.37 | 0.22 | 0.09 | 0.20 | 0.06 | 0.21 | -0.25 | 0.11 | **0.48** | 0.28 | -0.46 | 0.21 | 0.22 | 0.22 |
| *V* | | 1 | 0.82 | 0.11 | -0.46 | 0.31 | -0.17 | 0.53 | 0.12 | 0.30 | -0.19 | -0.51 | **0.88** | 0.57 | 0.08 | -0.40 | 0.02 | 0.54 | 0.19 |
| *Mn* | | | 1 | 0.11 | -0.31 | 0.39 | -0.10 | 0.17 | 0.31 | 0.10 | -0.11 | -0.21 | 0.15 | 0.56 | 0.20 | -0.54 | 0.01 | **0.84** | 0.43 |
| *Co* | | | | 1 | -0.11 | -0.07 | -0.13 | 0.47 | -0.14 | **0.53** | -0.10 | -0.37 | 0.18 | 0.07 | 0.44 | -0.70 | -0.08 | 0.10 | -0.19 |
| *Ni* | | | | | 1 | 0.68 | 0.93 | -0.44 | 0.08 | 0.12 | **0.93** | 0.18 | -0.34 | -0.33 | 0.28 | -0.22 | 0.80 | -0.02 | 0.04 |
| *Cu* | | | | | | 1 | 0.86 | 0.07 | -0.01 | 0.26 | 0.85 | -0.37 | -0.25 | 0.65 | 0.39 | -0.21 | **0.90** | 0.39 | 0.05 |
| *Zn* | | | | | | | 1 | -0.19 | -0.02 | 0.21 | **1.00** | -0.13 | -0.33 | 0.48 | 0.35 | 0.11 | 0.92 | 0.07 | -0.01 |
| *As* | | | | | | | | 1 | -0.61 | 0.29 | -0.20 | **-0.83** | 0.54 | 0.61 | 0.36 | -0.70 | 0.12 | -0.21 | -0.64 |
| *Yt* | | | | | | | | | 1 | 0.00 | -0.01 | 0.49 | 0.29 | -0.23 | -0.15 | -0.52 | -0.26 | 0.65 | **0.98** |
| *Cd* | | | | | | | | | | 1 | 0.23 | -0.31 | 0.62 | 0.38 | -0.01 | -0.28 | 0.26 | -0.01 | -0.02 |
| *Pb* | | | | | | | | | | | 1 | -0.12 | -0.33 | -0.69 | 0.35 | -0.48 | **0.90** | 0.07 | 0.00 |
| *Bi* | | | | | | | | | | | | 1 | -0.29 | -0.50 | -0.51 | 0.01 | -0.44 | 0.10 | **0.51** |
| *U* | | | | | | | | | | | | | 1 | 0.30 | -0.59 | -0.21 | -0.29 | -0.28 | 0.22 |
| *Pt* | | | | | | | | | | | | | | 1 | 0.31 | 0.17 | **0.64** | -0.36 | -0.36 |
| *Ru* | | | | | | | | | | | | | | | 1 | -0.16 | 0.42 | **0.52** | -0.26 |
| *Ir* | | | | | | | | | | | | | | | | 1 | **0.88** | -0.44 | -0.33 |
| *Pd* | | | | | | | | | | | | | | | | | 1 | 0.01 | -0.25 |
| *La* | | | | | | | | | | | | | | | | | | 1 | **0.74** |
| *Lu* | | | | | | | | | | | | | | | | | | | 1 |

**NOTE:** Correlation coefficients between −0.30 and 0.30 are considered to be insignificant, whereas more significant correlations are in bold

Table 8. REE compositions of samples from the Kurnalpi goldfield

| Sample ID | La | Ce | Pr | Nd | Sm | Eu | Gd | Tb | Dy | Ho | Er | Tm | Yb | Lu |
|---|---|---|---|---|---|---|---|---|---|---|---|---|---|---|
| 201929A | 12.1 | 29.8 | 2.4 | 8.5 | 1.9 | 0.6 | 2.1 | 0.3 | 1.7 | 0.3 | 1.0 | 1.0 | 0.1 | 12.1 |
| 201929B | 5.1 | 7.2 | 0.8 | 4.2 | 1.0 | 0.5 | 0.9 | 0.2 | 0.8 | 0.2 | 0.6 | 0.5 | 0.1 | 5.1 |
| 201929A-R | 27.2 | 70.1 | 5.3 | 17.5 | 4.3 | 2.1 | 7.9 | 0.8 | 4.7 | 1.0 | 5.8 | 3.7 | 0.7 | 27.2 |
| 201930A | 11.7 | 8.1 | 1.0 | 3.9 | 1.1 | 0.6 | 0.8 | - | - | - | 0.6 | - | 0.1 | 11.7 |
| 201930B | 7.6 | 12.1 | 1.4 | 5.1 | 1.9 | 0.6 | 1.8 | 0.3 | 2.3 | 0.5 | 1.5 | 1.6 | 0.2 | 7.6 |
| 201930C | 3.0 | 2.8 | 0.4 | 1.6 | 0.5 | 0.2 | 0.6 | 0.1 | 0.4 | 0.1 | 0.3 | 0.2 | 0.0 | 3.0 |
| 201943 | 10.7 | 9.8 | 1.6 | 7.4 | 1.3 | 0.4 | 1.6 | 0.3 | 1.1 | 0.3 | 0.7 | 0.6 | 0.1 | 10.7 |
| 201943-R | 3.0 | 4.0 | 0.6 | 2.5 | 0.5 | 0.2 | 0.7 | - | - | - | 0.4 | - | 0.1 | 3.0 |
| 201943-R1 | 10.6 | 20.0 | 2.1 | 7.4 | 1.9 | 0.9 | 3.9 | 0.6 | 3.6 | 0.7 | 4.2 | 2.3 | 0.4 | 10.6 |
| 201962A | 11.8 | 17.2 | 2.5 | 14.3 | 2.1 | 0.8 | 2.5 | 0.5 | 2.4 | 0.5 | 1.7 | 1.5 | 0.3 | 11.8 |
| 201962B | 6.8 | 11.8 | 1.4 | 6.0 | 1.3 | 0.5 | 1.9 | 0.2 | 1.2 | 0.2 | 0.7 | 0.6 | 0.1 | 6.8 |
| 201962A-R | 14.7 | 30.9 | 2.9 | 11.4 | 2.7 | 1.3 | 6.0 | - | - | - | 11.9 | - | 0.8 | 14.7 |

**NOTES:** -R suffix on the sample ID indicates a repeat analysis of the same sample; all measurements are in ppb

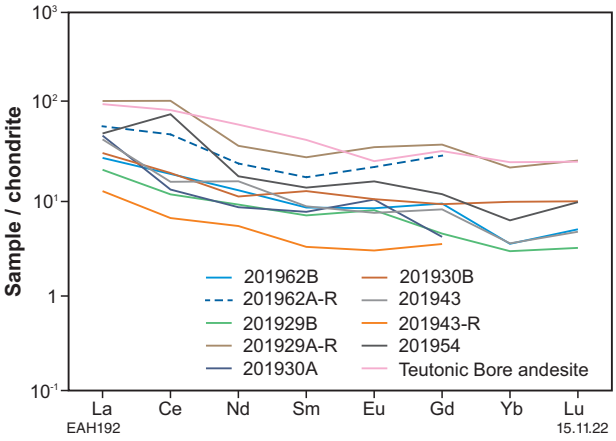


Figure 19. Chondrite-normalized REE for samples from the Kurnalpi goldfield. Dashed lines represent repeat analyses (-R). Data for Teutonic Bore andesite is shown for comparison (Park and Campbell, 2020)

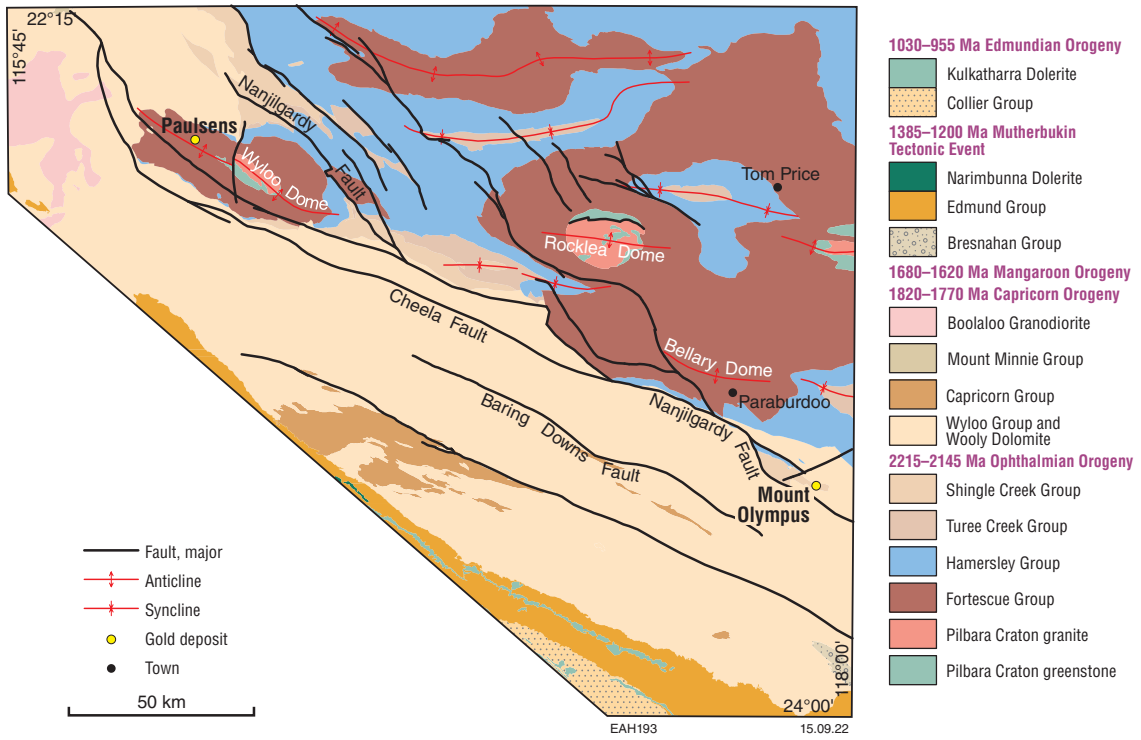


Figure 20. Geological map of the northern Capricorn Orogen showing locations of the Paulsens and Mount Olympus gold deposits (from Hancock and Thorne, 2016)

Table 9. Pb isotope composition and calculated source μ-values ($^{238}U/^{204}Pb$) for selected native gold samples from Mount Olympus and Paulsens deposits

| Sample ID | Deposit | $^{206}Pb/^{204}Pb$ | $^{207}Pb/^{204}Pb$ | $^{208}Pb/^{204}Pb$ | $Age_1$ (Ga) | $^{238}U/^{204}Pb_1$ | $Age_2$ (Ga) | $^{238}U/^{204}Pb_2$ |
|---|---|---|---|---|---|---|---|---|
| 201909-R | Paulsens | 17.402 ± 64 | 15.533 ± 58 | 36.872 ± 135 | 0.79 | 9.70 | 0.43 | 8.50 |
| 201912 | Olympus | 17.840 ± 23 | 15.564 ± 20 | 37.673 ± 49 | 0.52 | 9.68 | 0.12 | 8.51 |
| 201912-R | Olympus | 16.684 ± 16 | 15.481 ± 15 | 36.254 ± 36 | 1.24 | 9.83 | 0.92 | 8.51 |
| 201914C-R | Olympus | 15.972 ± 3 | 15.399 ± 3 | 35.530 ± 7 | 1.66 | 10.00 | 1.38 | 8.52 |

**NOTES:** -R suffix on the sample ID indicates a repeat analysis of the same sample. $Age_1$ and $(^{238}U/^{204}Pb)_1$ were calculated using the Stacey and Kramers (1975) model. $Age_2$ and $^{238}U/^{204}Pb_2$ were calculated using the Uchi–Wabigoon model for the Pilbara (Thorpe et al., 1992). Analytical uncertainty is standard deviation (SD)

All samples combined yield an imprecise isochron age of c. 1.4 Ga (1442 ± 230 Ma; MSWD = 2.3; Fig. 21). Considering only the least radiogenic Pb yields a model age of ~1.7 Ga, similar to the c. 1680 Ma age of younger mineralization at Paulsens (Fielding et al., 2017). Although imprecise, the Pb isotope data suggest that the younger generation of gold at Paulsens and the gold nuggets from Mount Olympus formed at about the same time. These data confirm that gold typically contains a small amount of U, which decays naturally over time. With low Pb samples, the Pb isotope composition evolves and, in this case, its adherence to an isochron (Fig. 20) suggests it has not been disturbed since formation at ~1.7 Ga.

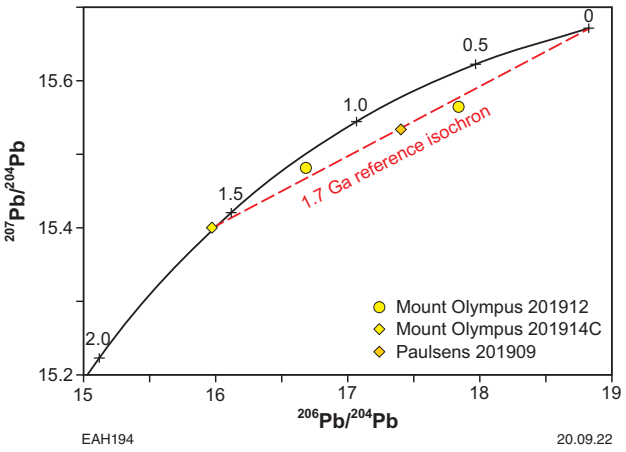


Figure 21. Plot of $^{207}Pb/^{204}Pb$ vs $^{206}Pb/^{204}Pb$ for samples from the Mount Olympus and Paulsens deposits, together with the Stacey and Kramer (1975) growth curve. A 1.7 Ga reference isochron is fitted through the samples with the least radiogenic Pb

## Re–Os and platinum group element systematics

The three gold samples yielded Re contents of 1.1 to 3.8 ppb and Os contents of 3.0 to 8.6 ppt (Table 10). All duplicate samples (batch 2) were of sufficient size to yield Os above the cutoff of 10% of blank concentration. The Os isotope composition is well below crustal values (Shirey and Walker, 1998), suggesting a deep, possibly magmatic, source of Os in ore fluid, without significant contamination from crust (possibly introduced via deep-seated faults).

The three samples contain 36 to 49 ppb Pt, 0.2 to 0.3 ppb Ru, 0.2 to 0.3 ppb Ir, and 0.6 to 0.9 ppb Pd (Table 11), similar to values for Kurnalpi gold (Table 6). The overall distribution of PGE is similar to those of older Archean nuggets (Kurnalpi; Fig. 16), with distinctive enrichment of Pt and Pd (P-PGE) over Ir, Os and Ru (I-PGE), with Pd/Os >> 1 (Fig. 22).

## Trace elements

The three gold samples (each with duplicates) were analysed for their trace elements (Appendix 3). Median abundances decrease in the following order (in ppm): Cu [490] → As [41] → Zn [18] → V [15] → Ti [8] → Ni [3] → Mn [1.7] → Co [1.6] → Pb [1.2] → Cd [0.3] → Bi [0.2]. Correlation coefficients have not been calculated because of the low number of analyses. However, the data represent primary mineralization and as such represent important data for comparison with gold nuggets sourced from other terranes.

Table 10. Re and Os elemental and isotope compositions of samples from the Mount Olympus and Paulsens deposits

| Sample ID | Deposit | Re (ppb) | Os (ppt) | $^{187}Re/^{188}Os$ | $^{187}Os/^{188}Os$ |
|---|---|---|---|---|---|
| 201909-R | Paulsens | 2.65 ± 0.14 | 3.0 ± 0.1 | 4287.8 ± 400.4 | 0.2889 ± 0.0428 |
| 201912-R | Olympus | 3.79 ± 0.17 | 4.5 ± 0.1 | 4081.9 ± 266.3 | 0.1712 ± 0.0244 |
| 201914C-R | Olympus | 1.09 ± 0.07 | 8.6 ± 0.0 | 621.5 ± 40.6 | 0.2377 ± 0.0059 |

**NOTE**: Analytical uncertainty is 2 sigma

Table 11. PGE compositions of samples from the Mount Olympus and Paulsens deposits

| Sample ID | Ir | 2σ | Ru | 2σ | Pt | 2σ | Pd | 2σ |
|---|---|---|---|---|---|---|---|---|
| 201909 | 0.22 | 0.12 | 0.36 | 0.15 | 39.13 | 1.07 | 0.65 | 0.03 |
| 201912 | 0.30 | 0.18 | 0.30 | 0.07 | 51.22 | 1.85 | 0.90 | 0.05 |
| 201914C | 0.32 | 0.14 | 0.20 | 0.10 | 52.74 | 1.56 | 0.57 | 0.03 |

**NOTES:** All measurements are in ppb. Analytical uncertainty is 2 sigma

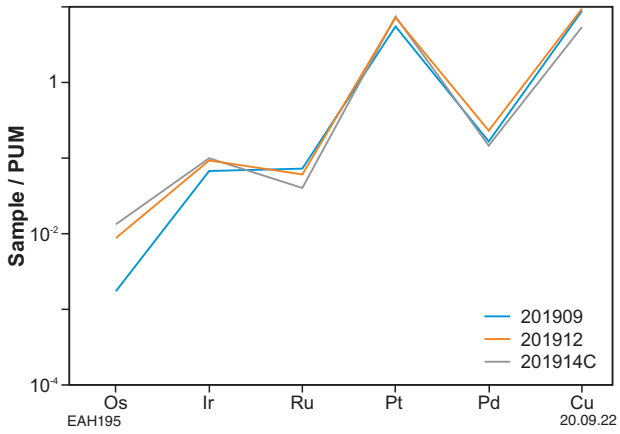


Figure 22. Primitive mantle-normalized PGE and Cu patterns for samples from the Mount Olympus and Paulsens deposits

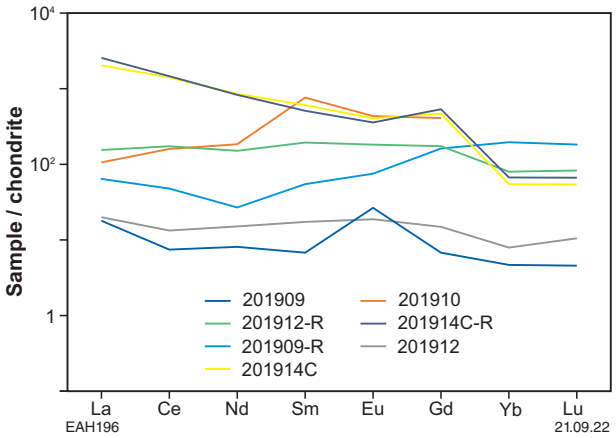


Figure 23. Chondrite-normalized REE variation diagram for samples from the Mount Olympus and Paulsens deposits. Dashed lines represent repeat analyses (-R)

# Rare earth elements

Concentrations of REE for the three samples are listed in Table 12 and shown in Figure 23. The REE contents vary by two orders of magnitude, although the overall patterns are similar. GSWA 201909 displays a significant Eu anomaly and minor Ce anomaly. An Eu anomaly is typical of hydrothermal sulfides (e.g. Rimskaya-Korsakova and Dubinin, 2003).

The introduction of REE into native gold can be similar to that for hydrothermal minerals and controlled by absorption and coprecipitation and by substitution of major cations in the mineral lattice (Morgan and Wandless, 1980). Eu in modern hydrothermal settings exhibits both positive (inherited from fluid) and negative anomalies (TAG and Broken Spur fields) (Rimskaya-Korsakova and Dubinin, 2003). In hydrothermal systems, the negative Eu anomaly is explained by a lower distribution coefficient between sulfide and fluid (Rimskaya-Korsakova and Dubinin, 2003). Thus, we consider that the REE in primary gold mineralization from these two Capricorn Orogen deposits preserves some characteristics of the ore-forming fluid.

Table 12. REE compositions of samples from the Mount Olympus and Paulsens deposits

| Sample ID | La | Ce | Pr | Nd | Sm | Eu | Gd | Tb | Dy | Ho | Er | Tm | Yb | Lu |
|---|---|---|---|---|---|---|---|---|---|---|---|---|---|---|
| 201909 | 4.2 | 4.5 | 0.6 | 3.7 | 1.0 | 1.5 | 1.3 | 0.2 | 1.3 | 0.3 | 0.7 | 0.8 | 0.1 | 4.2 |
| 201909-R | 15.0 | 28.8 | 3.2 | 12.2 | 8.1 | 4.2 | 31.8 | 8.3 | 59.1 | 12.8 | 42.9 | 31.8 | 4.4 | 15.0 |
| 201910 | 24.9 | 96.4 | 12.7 | 83.5 | 112.3 | 24.3 | 80.3 | 14.5 | 25.1 | 20.8 | 31.0 | – | – | 9.7 |
| 201912 | 4.7 | 8.0 | 1.2 | 6.8 | 2.6 | 1.1 | 2.9 | 0.6 | 3.0 | 0.6 | 1.6 | 1.3 | 0.3 | 4.7 |
| 201912-R | 36.3 | 104.3 | 15.3 | 68.3 | 28.5 | 10.2 | 34.1 | 5.4 | 29.9 | 5.2 | 20.5 | 13.0 | 2.0 | 36.3 |
| 201914C | 478 | 849 | 109 | 386 | 89 | 23 | 92 | 10 | 36 | 5.6 | 15.0 | 8.9 | 1.3 | 478 |
| 201914C-R | 599 | 883 | 117 | 375 | 75 | 20 | 105 | 9 | 38 | 6.2 | 18.7 | 10.9 | 1.6 | 599 |

**NOTES**: -R suffix on the sample ID indicates a repeat analysis of the same sample. All measurements are in ppb

# Pilbara Craton

Seven gold nuggets (Fig. 2) and galena inclusions from four gold samples (Fig. 3) from various locations in the Pilbara Craton were analysed in this study (Fig. 24 and Appendix 1).

## Geological setting

### Mosquito Creek, East Pilbara

Gold nuggets GSWA 247031 and 247032A were sourced from a quartz vein on a ridge in metasedimentary rocks at the Halcomes Peak prospect. The area is located on the southeastern side of the Mosquito Creek Basin – a rift basin formed between the East Pilbara and the Kurrana Terranes – in the 2980–2930 Ma Mosquito Creek Formation (Hickman, 2022a). The formation consists of a fault-imbricated sequence of turbiditic metasedimentary rocks and lesser mafic–ultramafic metavolcanic rocks (Hickman, 2022a).

### Marble Bar, East Pilbara

Four gold nuggets that comprise GSWA 201969 were collected from colluvium at the Coolyia Creek prospect in the Marble Bar Sub-basin, southwest of the Split Rock Shear Zone, close to Archean quartz reefs. Another gold nugget (GSWA 247016) was collected from colluvium at the Virgin Creek prospect. The colluvium overlies a cobble–boulder conglomerate unit of the 2766–2749 Ma Hardey Formation (Hickman, 2020) of the Fortescue Basin, and consists of well-rounded clasts of Mount Roe Basalt and granite in a matrix of quartzofeldspathic sand and mafic volcanic detritus.

### Mallina, Central Pilbara

GSWA 247009 was collected from a conglomerate unit at the base of the 2775–2772 Ma Mount Roe Basalt in the southern Mallina Basin within the Central Pilbara Tectonic Zone (Hickman and van Kranendonk, 2012). Metamorphosed interbedded shale, siltstone and sandstone of the 3015–2931 Ma Mallina Formation (Hickman, 2022b) also crops out nearby to the north and northeast.

### Silica Hills, West Pilbara

Samples GSWA 201978, 201981 and 201994 were collected from weathered metavolcanic rocks of the Tozer Formation at the Silica Hills prospect, in the Sholl greenstone belt of the Sholl Terrane, northwest Pilbara Craton. The 3128–3116 Ma Tozer Formation consists of metarhyolite and metadacite, in contact with metabasalt and basaltic meta-andesite (Hickman, 2021).

## Pb–Pb isotope systematics

### Marble Bar, East Pilbara

One galena inclusion (GSWA 247016) and four nuggets from GSWA 201969 (A–D) were analysed for Pb isotopes (Table 13). The galena inclusion has the least radiogenic Pb isotope composition of the sample suite ($^{206}Pb/^{204}Pb$ = 14.627; $^{207}Pb/^{204}Pb$ = 15.072), yielding a model age of c. 2.25 Ga. Four gold nuggets display much more radiogenic Pb isotope compositions, with $^{206}Pb/^{204}Pb$ of 16.699 to 19.494 (Fig. 25).

Assuming the galena preserves the initial Pb for the gold subsamples, all five data points form an isochron indicating an imprecise age of 2434 ± 260 Ma (MSWD = 0.66), within uncertainty of the imprecise model age for the galena. As with nuggets from other areas, we conclude that the current Pb isotope compositions are a combination of initial Pb (best gleaned from galena inclusions or Pb-rich gold samples) and in situ U decay. In this case the c. 2.25 Ga model age is considered the best estimate of the formation of the gold nuggets. This event is cryptically documented throughout the Pilbara as regional alteration events (i.e. c. 2.3 and 2.2 Ga; Rasmussen et al., 2020), including a phase of episodic formation of giant iron ore deposits (Rasmussen et al., 2007). The 2.3 Ga event may have been related to a protracted interval of deformation that affected the Fortescue, Hamersley and Turee Creek Groups prior to the 2.22 – 2.15 Ga Ophthalmia Orogeny (Rasmussen et al., 2020).

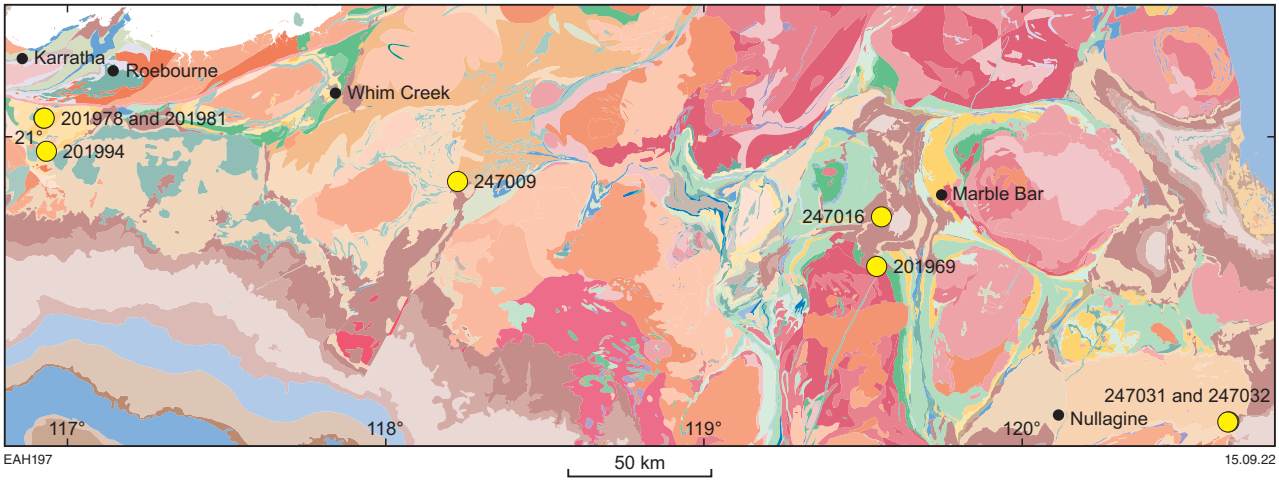


Figure 24. Geological map of a part of Pilbara Craton and locations of gold samples. Bedrock geology from GSWA (2020)

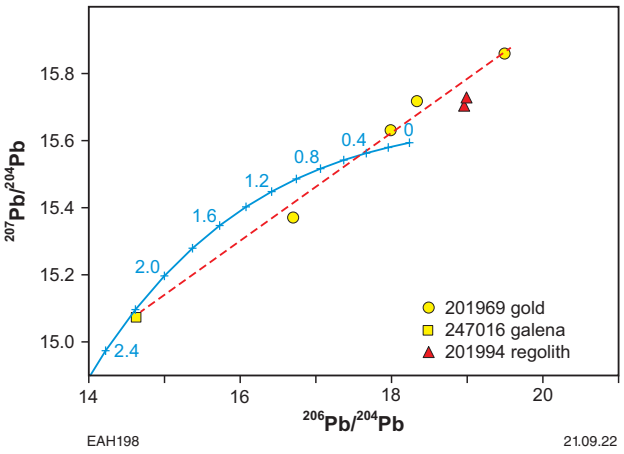


Figure 25. Plot of $^{207}Pb/^{204}Pb$ vs $^{206}Pb/^{204}Pb$ for samples from the Marble Bar area, East Pilbara, together with the Uchi–Wabigoon growth curve (Thorpe et al., 1992). Regolith gold analyses are from the West Pilbara

## Mosquito Creek, East Pilbara

Two analyses were conducted of a galena inclusion from sample GSWA 247032 (nugget A), and one analysis of native gold from sample GSWA 247031 (Table 13). The galena inclusion yielded $^{206}Pb/^{204}Pb$ ratios of 14.043 and 14.237, with corresponding Pb model ages of 2.66 and 2.60 Ga (Stacey and Kramers, 1975) or 2.53 and 2.44 Ga (Uchi–Wabigoon model). Gold nugget GSWA 247031 exhibits the least alteration, and yielded more radiogenic Pb, with a model age of 2.02 (Stacey and Kramers, 1975) or 1.77 Ga (Uchi–Wabigoon model).

These two data points for GSWA 247032 plot slightly above the Uchi–Wabigoon growth curve (Fig. 26), suggesting they could represent mixtures between initial Pb and more radiogenic Pb related to a younger event. This younger event could also have affected GSWA 247031, which indicated a model age of 2.02 Ga (Stacey and Kramers, 1975) or 1.77 (Uchi–Wabigoon model). The age of the younger event is unconstrained without more data, but could reflect the Capricorn Orogeny.

All three analyses plot above the growth curve (Fig. 26) and yield model ages much younger than their local host rocks. Their positions above the growth curve implies a significant interval of Pb evolution in a high-μ source, compatible with Pb having been derived from the older crustal rocks of the Pilbara. However, there is insufficient data to speculate further on either the timing of nugget formation or the Pb source.

## Silica Hills, West Pilbara

Analyses were conducted on one galena inclusion (GSWA 201978), two irregular gold samples from ferruginous regolith (GSWA 201981 and 201994), and on regolith material (GSWA 201994Reg) that hosts GSWA 201994 (Table 13). The galena inclusion yielded the least radiogenic Pb, with $^{206}Pb/^{204}Pb$ = 13.021, and model ages of 2.87 Ga (Stacey and Kramers, 1975) and 2.91 Ga (Uchi–Wabigoon model).

Table 13. Pb isotope compositions and source μ-values ($^{238}U/^{204}Pb$) for Pilbara samples

| *Sample ID* | *Material analysed* | *$^{206}Pb/^{204}Pb$* | *$^{207}Pb/^{204}Pb$* | *$^{208}Pb/^{204}Pb$* | *$Age_1$(Ga)* | *$^{238}U/^{204}Pb_1$* | *$Age_2$ (Ga)* | *$^{238}U/^{204}Pb_2$* |
|---|---|---|---|---|---|---|---|---|
| **East Pilbara** | | | | | | | | |
| *Mosquito Creek* | | | | | | | | |
| 247032 | Galena | 14.043 ± 4 | 14.942 ± 5 | 33.672 ± 11 | 2.66 | 10.96 | 2.53 | 9.04 |
| 247032-R | Galena | 14.237 ± 1 | 15.030 ± 1 | 33.842 ± 2 | 2.60 | 11.08 | 2.44 | 9.09 |
| 247031 | Gold | 15.681 ± 0 | 15.492 ± 0 | 35.241 ± 1 | 2.02 | 11.11 | 1.77 | 9.26 |
| *Marble Bar* | | | | | | | | |
| 247016 | Galena | 14.627 ± 59 | 15.072 ± 63 | 34.240 ± 169 | 2.29 | 9.968 | 2.19 | 8.88 |
| 201969A | Gold | 18.335 ± 37 | 15.718 ± 29 | 38.320 ± 70 | 0.46 | 10.23 | | |
| 201969B | Gold | 19.494 ± 40 | 15.860 ± 15 | 41.464 ± 66 | 1.39 | 10.03 | | |
| 201969C | Gold | 17.988 ± 40 | 15.631 ± 164 | 37.965 ± 420 | 0.54 | 9.94 | | |
| 201969D | Gold | 16.699 ± 113 | 15.370 ± 111 | 36.981 ± 275 | 1.03 | 9.21 | | |
| **Central Pilbara** | | | | | | | | |
| 247009 | Galena | 15.926 | 15.444 | 34.921 | 1.76 | 10.36 | 1.56 | 9.06 |
| **West Pilbara** | | | | | | | | |
| 201978 | Galena | 13.021 ± 10 | 14.348 ± 11 | 32.785 ± 23 | 2.87 | 8.74 | 2.91 | 8.59 |
| 201981 | Gold | 13.599 ± 19 | 14.550 ± 21 | 33.424 ± 48 | 2.48 | 8.02 | | |
| 201981-R | Gold | 14.043 ± 327 | 14.655 ± 369 | 33.978 ± 114 | 2.16 | 7.66 | | |
| 201994 | Gold | 16.332 ± 649 | 15.218 ± 636 | 36.277 ± 1.449 | 1.04 | 8.64 | | |
| 201994Reg | Regolith | 18.990 ± 54 | 15.729 ± 43 | 39.091 ± 114 | | | | |
| 201994Reg-R | Regolith | 18.960 ± 3 | 15.705 ± 2 | 39.009 ± 3 | | | | |

**NOTES:** -R suffix on the sample ID indicates a repeat analysis of the same sample. $Age_1$ and $(^{238}U/^{204}Pb)_1$ were calculated using the Stacey and Kramers (1975) model. $Age_2$ and $^{238}U/^{204}Pb_2$ were calculated using the Uchi–Wabigoon model for the Pilbara (Thorpe et al., 1992). Analytical uncertainty is standard deviation (SD)

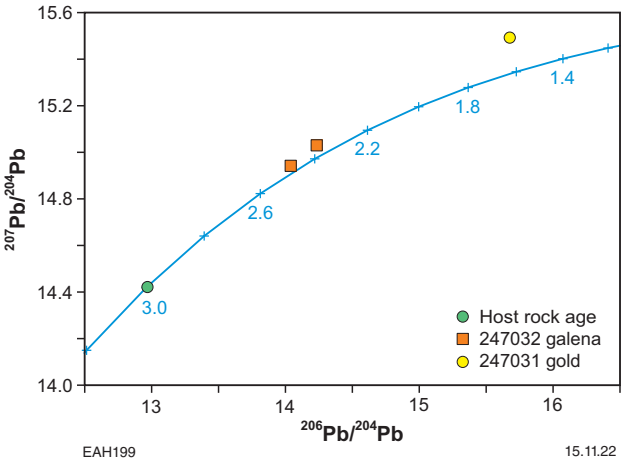


Figure 26. Plot of $^{207}Pb/^{204}Pb$ vs $^{206}Pb/^{204}Pb$ for samples from the Mosquito Creek area, East Pilbara, together with the Uchi–Wabigoon growth curve (Thorpe et al., 1992). Host rock age refers to the age of the 2980–2930 Ma Mosquito Creek Formation (Hickman, 2022b), which is considered as a maximum age for the gold

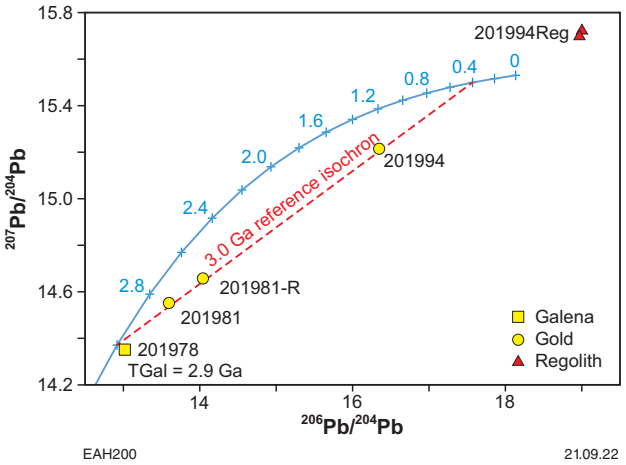


Figure 27. Plot of $^{207}Pb/^{204}Pb$ vs $^{206}Pb/^{204}Pb$ for samples from the West Pilbara, together with the Uchi–Wabigoon growth curve (Thorpe et al., 1992)

Two repeat analyses of native gold sample 201981 yield $^{206}Pb/^{204}Pb$ ratios of 13.599 and 14.043, which are more radiogenic than that for the galena inclusion. This demonstrates that the gold contains Pb ingrowth from U decay away from initial Pb (as interpreted from the galena results) and does not yield reliable age information. A 3.1 Ga reference isochron is shown with the data in Figure 27. If both nuggets had the same initial Pb, then an isochron age of c. 3.1 Ga might indicate their formation age. However, this assumption cannot be verified and the galena model age of ~2.9 Ga remains the best estimate of the formation age for one of the nuggets.

Gold sample GSWA 201994 displays radiogenic Pb ratios that plot well below the growth curve (Fig. 27), possibly due to U decay. Two analyses of ferruginous regolith hosting this gold displays the most radiogenic values in this study, with $^{206}Pb/^{204}Pb$ of 18.960 and 18.990 and $^{207}Pb/^{204}Pb$ ratios of 15.705 and 15.729 (Fig. 27). These data plot on a continuation of the Pb growth curve close to present day Pb isotope composition estimate according to the Stacey and Kramers model ($^{206}Pb/^{204}Pb$ = 18.700; $^{207}Pb/^{204}Pb$ = 15.628; Stacey and Kramers, 1975). U content in a regolith is 0.3 ppm (Appendix 3), with a U/Pb ratio of 0.06, further indicating that radiogenic decay of U contributed to the radiogenic Pb composition.

## Mallina, Central Pilbara

Only one galena inclusion was analysed from sample GSWA 247009 (Table 13), displaying radiogenic Pb ratios, with $^{206}Pb/^{204}Pb$ = 15.926. Data for this sample plots above the Pb growth curve, suggesting a complex (possibly post-burial) history and/or a source with a high U/Pb ratio, possibilities that need investigation with additional samples.

# Re–Os and platinum group element systematics

Re and Os abundances and isotope compositions were analysed in seven samples, although only one that returned Os contents >10% (17.4 ppt) above the blank values is listed in Table 14. The $^{187}Os/^{188}Os$ ratio is 0.845. The Re content in Mosquito Creek sample GSWA 247031 is 1.1 ppb.

Sample GSWA 247031 from Mosquito Creek yields a radiogenic $^{187}Os/^{188}Os$ ratio of 0.845, with the time of separation from mantle ($T_{MA}$) estimated at c. 131 Ma. This young age could potentially reflect the latest alteration event to have affected the sample.

PGE concentrations are relatively homogeneous, with 0.57 – 0.90 ppb Pd, 36 – 49 ppb Pt, 0.15 – 0.31 ppb Ru, and 0.22 – 0.30 ppb Ir (Table 15). The PGE patterns overall are similar to those for primary gold ores at the Paulsens deposit (Fig. 28), with enrichment in I-PGE (Os, Ir and Ru) for selected samples. However, all patterns are distinctly different to those for Witwatersrand gold documented by Schaefer et al. (2010), particularly in Pt/Pd (Fig. 27). The origin of this difference may relate to a different mode of formation of nuggets in the Witwatersrand Basin compared to those in the Pilbara Craton.

# Trace elements

Seven samples were analysed for trace elements in solution, including one repeat (Appendix 3, Fig. 29). Correlation coefficients are shown in Table 16. Median abundances of trace elements decrease in the order (in ppm): Cu [261] → As [49] → Zn [27] → V [15] → Ti [14] → Mn [9] → Ni [3] → Pb [2] → Bi [0.5] → Co [0.3] → Cd [0.1] → U [0.02], similar to data for the Kurnalpi goldfield. Maximum Cu, Zn and As abundances are found in GSWA 201969C, which has a deformed polycrystalline structure.

Table 14. Re and Os elemental and isotope compositions of Pilbara samples

| *Sample ID* | *Re (ppb)* | *Os (ppt)* | *$^{187}Re/^{188}Os$* | *$^{187}Os/^{188}Os$* | *$T_{MA}$ (Ma)* |
|---|---|---|---|---|---|
| 247031 | 1.10 ± 0.03 | 17.4 ± 0.1 | 331 ± 9 | 0.845 ± 0.009 | 131 |

**NOTES:** -R suffix on the sample ID indicates a repeat analysis of the same sample. $T_{MA}$ refers to the age of separation from mantle. Analytical uncertainty is 2 sigma

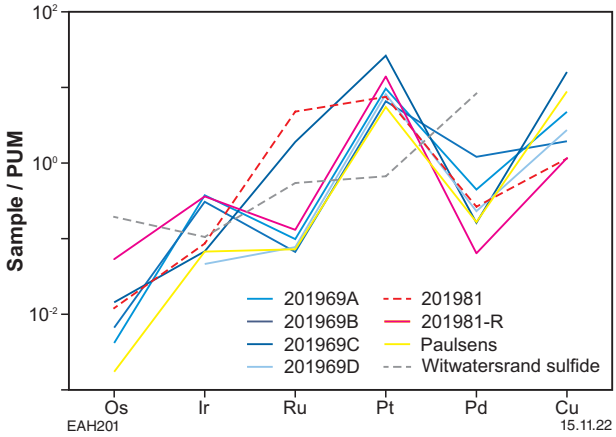


Figure 28. Primitive mantle-normalized PGE and Cu patterns for samples from the Pilbara. Data for the Paulsens samples (this Report) and Witwatersrand sulfide (Schaefer et al., 2010) are shown for comparison

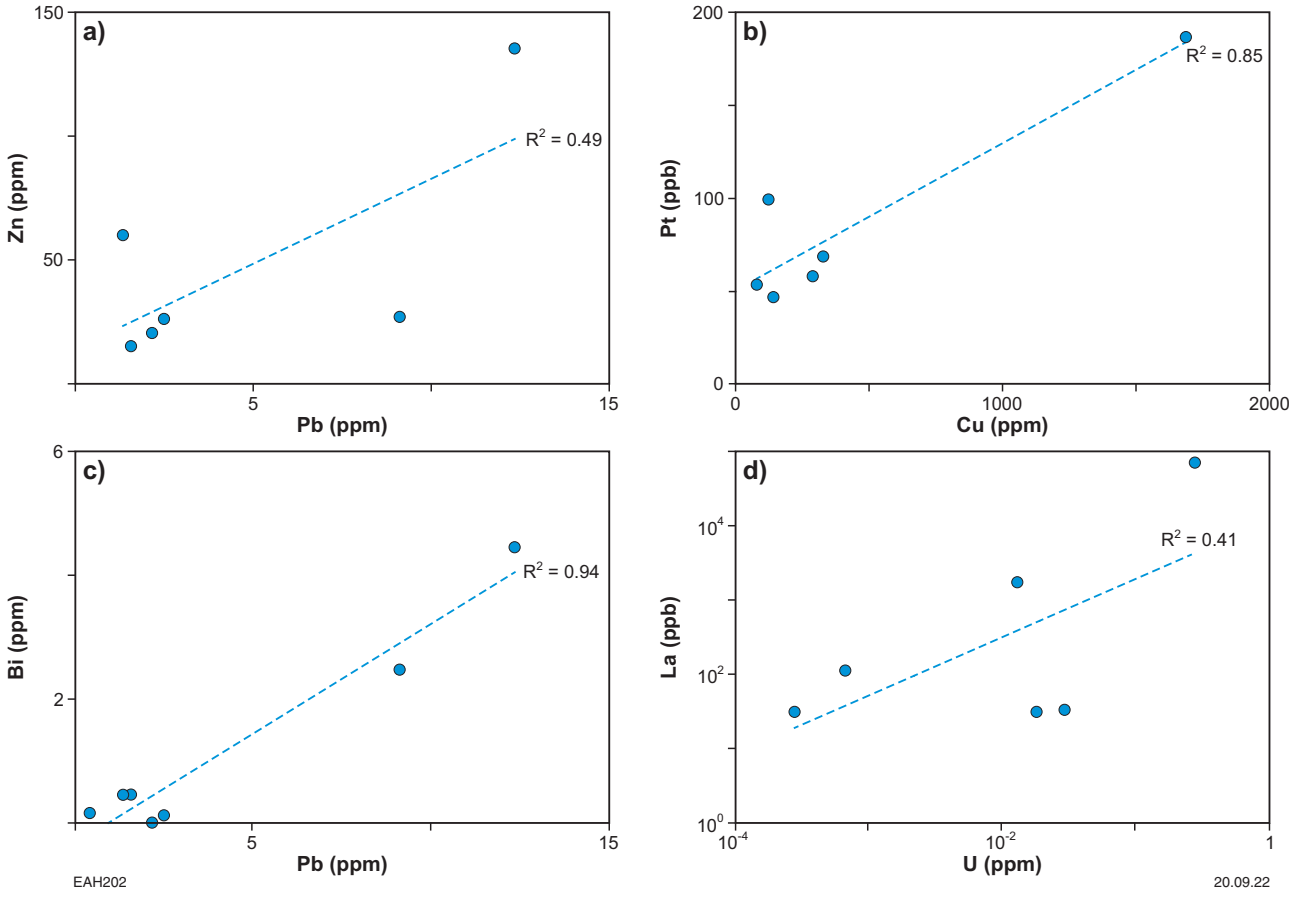


Figure 29. Trace element concentrations for samples from the Pilbara Craton (Table 16). $R^2$ = correlation coefficient

Table 15. PGE compositions of Pilbara samples

| *Sample ID* | *Ir* | *2σ* | *Ru* | *2σ* | *Pt* | *2σ* | *Pd* | *2σ* |
|---|---|---|---|---|---|---|---|---|
| 201969A | 1.20 | 0.26 | 0.49 | 0.16 | 68.47 | 1.84 | 1.74 | 0.09 |
| 201969B | 0.98 | 0.14 | 0.33 | 0.07 | 46.56 | 2.44 | 4.71 | 0.24 |
| 201969C | 0.22 | 0.10 | 9.52 | 0.88 | 186.59 | 7.37 | 0.63 | 0.03 |
| 201969D | 0.15 | 0.06 | 0.39 | 0.08 | 57.83 | 1.08 | 0.90 | 0.04 |
| 201981 | 0.28 | 0.17 | 23.93 | 5.87 | 53.26 | 1.06 | 1.03 | 0.05 |
| 201981R | 1.16 | 0.10 | 0.65 | 0.14 | 99.10 | 2.55 | 0.25 | 0.01 |

**NOTES:** -R suffix on the sample ID indicates a repeat analysis of the same sample. All measurements are in ppb.
Analytical uncertainty is 2 sigma

Table 16. Correlation coefficients between trace elements (including PGE and some REE) for Pilbara samples

| | *Ti* | *V* | *Mn* | *Co* | *Ni* | *Cu* | *Zn* | *As* | *Yt* | *Cd* | *Pb* | *Bi* | *U* | *Pt* | *Ru* | *Ir* | *Pd* | *La* | *Lu* |
|---|---|---|---|---|---|---|---|---|---|---|---|---|---|---|---|---|---|---|---|
| ***Ti*** | 1 | 0.78 | 0.60 | 0.83 | **0.89** | 0.32 | -0.22 | **0.98** | 0.80 | -0.20 | -0.39 | -0.26 | 0.86 | 0.22 | -0.15 | 0.03 | 0.50 | 0.81 | 0.02 |
| ***V*** | | 1 | 0.72 | 0.35 | 0.45 | **0.83** | -0.10 | 0.73 | 0.28 | 0.17 | -0.52 | -0.36 | 0.39 | 0.76 | -0.02 | -0.16 | 0.04 | 0.30 | -0.21 |
| ***Mn*** | | | 1 | 0.42 | 0.44 | 0.54 | 0.35 | 0.63 | 0.40 | 0.66 | -0.08 | 0.07 | 0.38 | 0.36 | 0.45 | -0.17 | -0.02 | 0.38 | 0.01 |
| ***Co*** | | | | 1 | 0.97 | -0.17 | -0.34 | 0.90 | **0.98** | **-0.32** | -0.27 | -0.19 | **0.997** | -0.32 | -0.28 | 0.30 | 0.73 | 0.999 | 0.01 |
| ***Ni*** | | | | | 1 | -0.09 | -0.33 | 0.94 | **0.97** | -0.35 | -0.40 | -0.29 | **0.99** | -0.22 | -0.26 | 0.26 | 0.70 | **0.96** | 0.15 |
| ***Cu*** | | | | | | 1 | 0.04 | 0.25 | -0.27 | 0.43 | -0.39 | -0.32 | -0.16 | **0.92** | 0.09 | -0.42 | -0.25 | -0.22 | -0.35 |
| ***Zn*** | | | | | | | 1 | -0.28 | -0.22 | 0.70 | **0.70** | **0.81** | -0.37 | 0.04 | -0.35 | -0.55 | -0.48 | -0.35 | 0.79 |
| ***As*** | | | | | | | | 1 | **0.86** | -0.22 | -0.51 | **-0.35** | **0.91** | 0.12 | -0.20 | 0.11 | 0.57 | 0.87 | 0.07 |
| ***Yt*** | | | | | | | | | 1 | -0.32 | -0.21 | -0.11 | **0.98** | -0.39 | -0.17 | 0.27 | 0.70 | 0.98 | **0.21** |
| ***Cd*** | | | | | | | | | | 1 | 0.31 | 0.37 | -0.44 | 0.33 | **0.74** | -0.30 | -0.59 | -0.34 | -0.03 |
| ***Pb*** | | | | | | | | | | | 1 | **0.97** | -0.38 | -0.24 | 0.65 | -0.04 | -0.56 | -0.26 | 0.16 |
| ***Bi*** | | | | | | | | | | | | 1 | -0.27 | -0.18 | 0.77 | -0.14 | -0.53 | -0.19 | 0.33 |
| ***U*** | | | | | | | | | | | | | 1 | -0.27 | -0.31 | 0.29 | 0.73 | **0.99** | 0.17 |
| ***Pt*** | | | | | | | | | | | | | | 1 | 0.07 | -0.25 | -0.48 | -0.37 | -0.42 |
| ***Ru*** | | | | | | | | | | | | | | | 1 | -0.55 | -0.46 | -0.29 | 0.80 |
| ***Ir*** | | | | | | | | | | | | | | | | 1 | -0.05 | 0.30 | -0.23 |
| ***Pd*** | | | | | | | | | | | | | | | | | 1 | 0.75 | -0.06 |
| ***La*** | | | | | | | | | | | | | | | | | | 1 | 0.22 |
| ***Lu*** | | | | | | | | | | | | | | | | | | | 1 |

**NOTE:** Correlation coefficients between −0.30 and 0.30 are considered to be insignificant, whereas more significant correlations are in bold

This sample also returned the highest Cu abundance (579 ppm) among Pilbara samples by the LA-ICP-MS method. The samples with high Cu contents also have high Pt, Cd and V, which suggests a statistical association between these elements (Table 16). The correlation coefficients calculated for Cu decrease in the following order: Cu → Pt → V → Cd (0.92 → 0.83 → 0.43 correspondingly). For Pb, a similar range has been calculated: Pb → Bi → Zn → Ru (0.97 → 0.70 → 0.65 correspondingly). A significant positive correlation between U and La ($R^2$ = 0.99) (Table 16) possibly indicates that a major part of U comes from microscopic silicate inclusions. These correlation coefficients, however, should be treated with caution due to the limited data available, and could be complemented by additional studies.

## Rare earth elements

Concentrations of REE are listed in Table 17 and patterns shown in Figure 30. Some samples (e.g. GSWA 201969B) display 2–3 orders of magnitude higher REE abundances than others. The similar REE pattern of sample GSWA 201969B to the regolith (red dotted line) suggests that this gold was recrystallized in the regolith environment (Appendix 1) and most likely preserved some trace elements from the surrounding regolith during recrystallization. In general, characteristic features include a pronounced Eu anomaly (similar to primary mineralization from Capricorn Orogen) and enrichment in light REE relative to heavy REE.

# Discussion and conclusions

## Pb systematics

A significant outcome of this study is demonstration that many native gold nuggets partially or completely preserve their initial Pb isotope compositions and hence their model ages can be considered reliable. Although model Pb ages are intrinsically imprecise due to the differences in current Pb isotope growth models, they are sufficient to demonstrate the approximate timing of placer gold nugget formation, as evidenced by model ages compatible with the ages of epigenetic gold ores in the local terrain. Importantly, some nuggets contain inclusions of galena that can be analysed efficiently for their Pb isotope compositions alone, providing reliable model ages.

In gold nuggets without galena inclusions, or with low Pb contents, the low amount of U present within gold leads to the ingrowth of radiogenic Pb, which allows for Pb–Pb isochrons to be defined from multiple analyses of a single nugget. However, in some instances, evidence of younger disturbance and gold recrystallization complicates data interpretation. Importantly, with low Pb contents in gold, sufficient sample is required for dissolution analysis to overcome the influence of blank contributions and to improve analytical precision; a minimum sample weight of 100 mg is recommended.

Table 17. REE compositions of Pilbara samples

| *Sample ID* | *La* | *Ce* | *Pr* | *Nd* | *Sm* | *Eu* | *Gd* | *Tb* | *Dy* | *Ho* | *Er* | *Tm* | *Yb* | *Lu* |
|---|---|---|---|---|---|---|---|---|---|---|---|---|---|---|
| 201969A | 31 | 26 | 3 | 16 | 3 | 1 | 3 | 0 | 1 | 0 | 1 | 1 | 0 | 31 |
| 201969B | 70 116 | 210 188 | 22 902 | 88 283 | 17 710 | 3 754 | 15 626 | 328 | 3 940 | 289 | 1 305 | 500 | 14 | 70 116 |
| 201969C | 33 | 57 | 7 | 27 | 8 | 3 | 12 | 2 | 11 | 2 | 8 | 9 | 1 | 33 |
| 201969D | 1 727 | 2 092 | 149 | 495 | 63 | 35 | 75 | 5 | 15 | 2 | 7 | 4 | 0 | 1 727 |
| 201981 | 112 | 197 | 29 | 119 | 49 | 11 | 138 | 31 | 230 | 55 | 176 | 206 | 31 | 112 |
| 201981-R | 31 | 45 | 7 | 28 | 13 | 3 | 24 | 5 | 33 | 7 | 21 | 20 | 3 | 31 |
| 247031 | 32 | 56 | 23 | 4 | 1 | 3 | 0 | 0 | 32 | 56 | 23 | 4 | 1 | 3 |
| 201994 | 253 | 883 | 135 | 798 | 772 | 784 | 534 | 102 | 487 | 131 | 256 | 62 | 41 | 253 |
| 201994Reg | 7 858 | 15 745 | 2 054 | 8 458 | 1 994 | 676 | 2 221 | 390 | 2 377 | 498 | 1 485 | 1 320 | 194 | 7 858 |

**NOTES:** -R suffix on the sample ID indicates a repeat analysis of the same sample. All measurements are in ppb

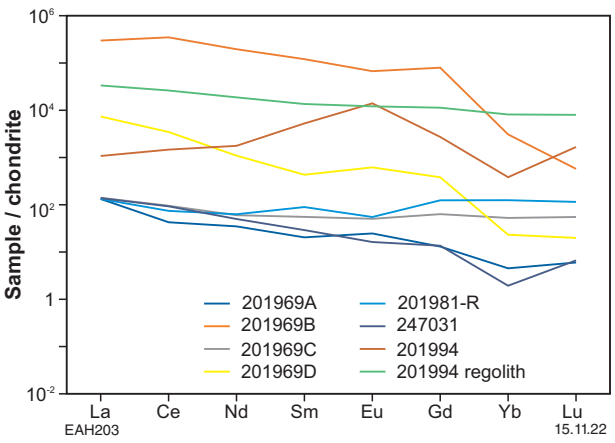


Figure 30. Chondrite-normalized REE variation diagram for samples from the Pilbara Craton

The most radiogenic nuggets display textural evidence of younger alteration events. A direct correlation is observed between Pb isotope composition and trace element content (Fig. 11), suggesting that younger alteration events may also be responsible for input of some trace elements (e.g. U). Some studied gold samples have a prolonged history of separation from their original source deposit and/or have complex burial histories. If significant Pb is added during secondary events, the Pb isotope composition potentially can establish the approximate age(s) of these events, via the determination of Pb–Pb isochrons. Interestingly, the youngest Pb model age established in this study (c. 300 Ma) approximates the Carboniferous–Permian glaciation event in Australia.

## Re–Os and platinum group element systematics

The limitation of sample size available for this project hindered the interpretation of Re–Os data. The analysed gold samples clearly have mantle-like $^{187}Os/^{188}Os$ ratios, which unequivocally indicates mantle Os within the gold, irrespective of the crustal pathway to the gold deposition site (i.e. through older or younger crust). A mantle source for Os within gold contrasts with Pb–Sr–Nd isotope studies of ore-associated minerals in Archean gold deposits, which consistently indicate a crustal source for these elements. However, Re–Os systematics is the only isotopic tracer system for which the crust has little daughter isotope to contaminate a mantle-derived ore fluid (as opposed to the Pb, Sr and Nd isotope systems). Our results demonstrate the potential, with more data, to finally provide a firm answer for the source of the ore fluid (and gold) in lode gold deposits. Note that there are already strong, yet still non-definitive arguments, for a mantle source of ore fluids for lode gold deposits from Archean to Recent within the literature (e.g. Groves et al., 2020). Furthermore, the unusually unradiogenic Os isotope composition, with an $^{187}Os/^{188}Os$ ratio between 0.1 and 0.2 in the majority of samples studied, indicates an unradiogenic Os source more consistent with magmatic input, without significant crustal influence. A similar conclusion was reached by Mueller et al. (2008) for genesis of the Granny Smith gold deposit in the Eastern Goldfields.

Concentrations of PGE (Os, Pt, Pd, Ru and Ir) are consistently low for most selected samples (i.e. below primitive mantle) (PUM; Fig. 31) and are slightly elevated for the Pilbara gold nuggets GSWA 201969 (Marble Bar) and GSWA 201981 (Silica Hills) (Fig. 31). From this preliminary study, the PGE patterns in native gold are similar to that for reference andesite and thus may provide a robust fingerprint preserved from their source due to their apparent resistance to later modification.

## Trace elements systematics

Most selected gold samples were originally analysed for their chemical composition using LA-ICP-MS (Hancock and Thorne, 2016; Hancock and Beardsmore, 2020), and their values in parts per million were calculated against certified gold RM (excluding samples from the Paulsens and Mount Olympus deposits, where results are reported in counts per second only). The laser spot and traverse data show that only Ag, Cu and Hg are consistently present in all gold samples (Appendix 1) in concentrations above LA-ICP-MS detection limits, and they probably occur as limited solid solutions within gold alloy. Other elements appear sporadically in low concentrations (sub-ppm levels), possibly as unobserved micro- and nano-inclusions. In contrast, lithophile elements (e.g. Mg, Al, Fe, Ti, V, Mn, Ba) are unlikely to occur in solid solution in gold and are considered to be contaminants from the surrounding rocks and external inclusions located in gold open voids, cracks and fissures. These elements are distinguished from trace elements derived from micro-inclusions by their consistently high concentrations in small gold grains as opposed to their absence in larger ones.

In the current study, gold samples were dissolved in acids to determine very low (in ppb and ppt) concentrations of REE and PGE and, in addition, the presence of other trace elements. Where available, the results were calibrated using verified gold RM (Appendix 3). The processed data are compared with available laser ablation data for Cu concentrations only, because Ag and Hg were excluded from this study and the majority of other elements reported herein have concentrations below LA-ICP-MS detection limits.

Cu contents analysed in solution for many samples are about two times higher than those analysed by the LA-ICP-MS technique (Fig. 32). A possible explanation is the occurrence of sub-microscopic inclusions containing Cu (e.g. chalcopyrite, galena, cobaltite), which were excluded from calculation during laser ablation data reduction. As expected from the larger amounts of sample material, the concentrations of lithophile elements in solution are higher than indicated by their corresponding laser ablation traverse data (e.g. Ti and Mn). Moreover, REE contents are elevated in gold sample solutions contaminated with regolith material in the form of macro- and micro-inclusions (see Fig. 30). A unique example of that is GSWA 201969B (Marble Bar), which has extremely high contents of REE (hundreds of ppm) that were most likely derived from surrounding regolith material during supergene recrystallization (Appendix 1).

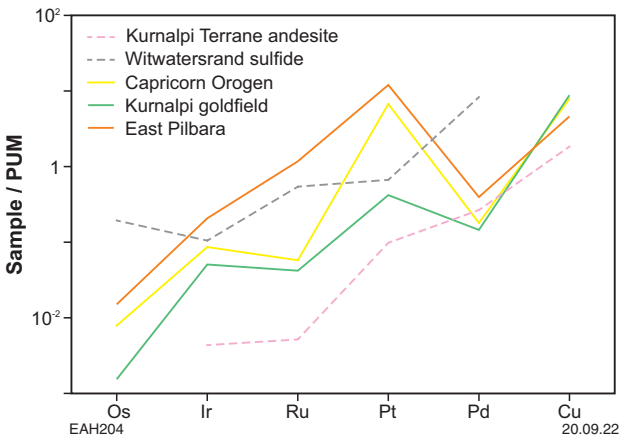


Figure 31. Primitive mantle-normalized PGE and Cu average patterns for gold from the Capricorn Orogen, Kurnalpi goldfield and East Pilbara. The andesite from the Kurnalpi Terrane (Park and Campbell, 2020) and sulfide from the Witwatersrand (Schaefer et al., 2010) are shown for comparison

Another sample (GSWA 201969D) from the same location contains elevated REE and also shows multiple traces of Mg, As, Zn, Se and Cr detected by LA-ICP-MS. Similar examples of gold nuggets capturing REE and other trace elements from surrounding rocks during local recrystallization are illustrated in samples GSWA 201914C (Mount Olympus) and GSWA 201994 (West Pilbara).

Overall, trace element data from the LA-ICP-MS and solution-ICP-MS methods represent different sampling scales. The LA-ICP-MS analysis can be directed to avoid inclusions and imperfections on a polished surface of gold, whereas dissolution of a larger sample will include an unknown and variable amount of inclusions, and likely include more recrystallized material, which appears to have higher trace element contents. As such, both methods have a role to play in fingerprinting gold geochemistry, although the low detection level advantage of the solution method does also introduce additional information and complexity to interpretation.

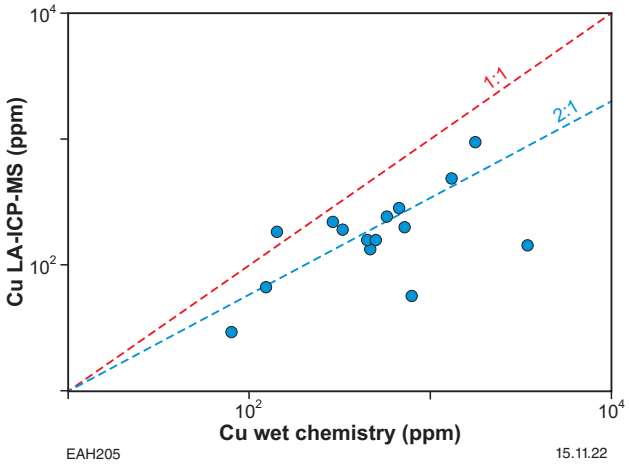


Figure 32. Comparison of Cu abundances in gold samples measured at JdLC using the wet chemistry/ICP-MS method vs Cu contents measured using LA-ICP-MS (GSWA data)

# Recommendations and future work

The acquisition of Pb isotopes from galena inclusions in native gold provides a simple, efficient and non-destructive technique to determine Pb model ages, which appear to be reliable, although model-sensitive. Table 18 shows that up to 22% of all nuggets from the Pilbara (where there is currently high exploration activity for conglomerate-hosted gold) assessed so far may contain galena inclusions. Due to this high exploration activity and the high abundance of galena inclusions within gold nuggets, Pb isotope age data could be very useful to guide exploration models and future exploration success.

Sample size is important. This project generally utilized gold samples <10 mg in weight, with resulting problems with high blank/sample ratios and insufficient Pb for precise Pb isotope analysis. We recommend 100 mg as a minimum sample size in future work. In situ U decay in Pb-poor native gold nuggets can generate Pb–Pb isochrons provided all samples had the same initial Pb. This assumption can be confirmed by analysing multiple sites on a single nugget, for which we recommend a proportion of the nuggets be >1–2 g to facilitate.

Lastly, the project was dominantly based on placer nuggets. To properly characterize primary gold from known ore deposits, a proportion of samples should come from well-characterized ores, especially from the areas where the age is poorly known.

Future studies should include collection of a greater proportion of primary native gold samples from ore deposits; their analysis for Pb isotopes will enable potential gold sources to be better characterized. Additional Pb isotope analysis could be conducted on nuggets currently available that contain galena inclusions. The collection and preparation of additional nuggets in the search for those with galena inclusions should be increased, particularly in the Pilbara and in collaboration with interested industry partners and through access to existing collections. Future studies should be based on a minimum sample weight of gold of ~100 mg and further assessment of Pb–Pb isochrons determined by multiple analyses on larger (>1–2 g) nuggets.

Future Re–Os and PGE analyses would benefit from additional Re–Os analysis on larger sample sizes of native gold (i.e. >100 mg) from primary ore samples from gold deposits with varied crustal pathways to assess crustal contamination of potential mantle-derived ore fluids: for example, nuggets from Pilbara vs Yilgarn vs Proterozoic host rocks.

Table 18. Gold samples curated by GSWA

| | *Kurnalpi* | *Paulsens* | *Mount Olympus* | *Pilbara* |
|---|---|---|---|---|
| Samples available | 75 | Gold particles from 6 samples | 4, plus gold particles from 2 samples | 106 |
| Samples prepared and assessed | 60 | This Report | This Report | 106 |
| Gold nuggets with galena inclusions | 4 | 0 | 0 | 23 |

**NOTES:** Information is current as of December 2021. Additional collections of native gold nuggets curated by GSWA and other WA government entities were not available to be counted in the current compilation

# References


Barrote, VR, Tesalina, SG, McNaughton, NJ, Jourdan, F, Hollis, SP, Ware, B and Zi, J-W 2020a, 4D history of the Nimbus VHMS ore deposit in the Yilgarn Craton, Western Australia: Precambrian Research, v. 337, article no. 105536.

Barrote, VR, McNaughton, NJ, Tessalina, SG, Evand, NJ, Talavera, C, Zi, J-W and McDonald, BJ 2020b, The 4D evolution of the Teutonic Bore Camp VHMS deposits, Yilgarn Craton, Western Australia: Ore Geology Reviews, v. 120, article no. 103448.

Birck, JL, Roy-Barman, M and Capman, F 1997, Re-Os isotopic measurements at the femtomole level in natural samples: Geostandards Newsletter, v. 21, p. 19–27, doi:10.1111/j.1751-908X.1997.tb00528.x.

Browning, P, Groves, DI, Blockley, JG and Rosman, KJR 1987, Lead isotope constrains on the age and source of gold mineralization in the Archean Yilgarn Block, Wastern Australia: Economic Geology, v. 82, p. 971–986.

Caruso, S, Fiorentini, ML, Hollis, SP, LaFlamme, C, Baumgartner, RJ, Steadman, JA and Savard, D 2018, The fluid evolution of the Nimbus Ag-Zn-(Au) deposit: an interplay between mantle plume and microbial activity: Precambrian Research, v. 317, p. 211–229.

Chen, M, Campbell, IH, Xue, Y, Tian, W, Ireland, TR, Holden, P, Cas, RAF, Hayman, PC and Das, R 2015, Multiple sulfur isotope analyses support a magmatic model for the volcanogenic massive sulfide deposits of the Teutonic Bore Volcanic Complex, Yilgarn Craton, Western Australia: Economic Geology, v. 110, p. 1411–1423.

Cohen, AS and Waters, FG 1996, Separation of osmium from geological materials by solvent extraction for analysis by thermal ionisation mass spectrometry: Analytica Chimica Acta, v. 332, p. 269–275.

Cumming, GL and Richards, JR 1975, Ore lead isotope ratios in a continuously changing Earth: Earth and Planetary Science Letters, v. 28, p. 155–171.

Esser, BK and Turekian, KK 1993, The osmium isotopic composition of the continental crust: Geochimica et Cosmochimica Acta, v. 57, no. 13, p. 3093–3104, doi:10.1016/0016-7037(93)90296-9.

Eyles, N and Broekert, P de 2001, Glacial tunnel valleys in the Eastern Goldfields of Western Australia cut below the late Paleozoic Pilbara ice sheet: Palaeogeography, Palaeoclimatology, Palaeoecology, v. 171, p. 29–40.

Fielding, IOH, Johnson, SP, Zi, J-W, Rasmussen, B, Muhling, JR, Dunkley, DJ, Sheppard, S, Wingate, MTD and Rogers, JR 2017, Using in situ SHRIMP U-Pb monazite and xenotime geochronology to determine the age of orogenic gold mineralization: an example from the Paulsens Mine, southern Pilbara Craton: Economic Geology, v. 112, p. 1205–1230.

Geological Survey of Western Australia 2020, 1:500 000 Interpreted bedrock geology of Western Australia, 2020: Geological Survey of Western Australia; data layer, <https://dasc.dmirs.wa.gov.au>.

Groves, DI, Goldfarb, RJ, Gebre-Mariam, M, Hagemann, SG and Robert, F 1998, Orogenic gold deposits: a proposed classification in the context of their crustal distribution and relationship to other gold deposit types: Ore Geology Reviews, v. 13, no. 1–5, p. 7–27.

Groves, DI, Santosh, M, Deng, J, Wang, Q, Yang, L and Zhang, L 2020, A holistic model for the origin of orogenic gold deposits and its implications for exploration: Mineralium Deposita, v. 55, no. 2, p. 275–292, doi:10.1007/s00126-019-00877-5.

Hancock, EA and Thorne, A 2011, Mineralogy of lode and alluvial gold from the western Capricorn Orogen, Western Australia: Australian Journal of Earth Sciences, v. 58, p. 793–801.

Hancock, EA and Thorne, AM 2016, Mineralogy of gold from the Paulsens and Mount Olympus deposits, northern Capricorn Orogen, Western Australia: Geological Survey of Western Australia, Record 2016/14, 16p.

Hancock, EA and Beardsmore, TJ 2020, Provenance fingerprinting of gold from the Kurnalpi goldfield: Geological Survey of Western Australia, Report 212, 21p.

Hickman, AH 2020, Hardey Formation (A-FOh-scb): Geological Survey of Western Australia, WA Geology Online, Explanatory Notes extract, viewed 6 April 2022, <www.dmirs.wa.gov.au/ens>.

Hickman, AH 2021, Tozer Formation (A-WHt-xb-f): Geological Survey of Western Australia, WA Geology Online, Explanatory Notes extract, viewed 22 June 2022, <www.dmirs.wa.gov.au/ens>.

Hickman, AH 2022a, Mosquito Creek Formation (A-NUq-mh): Geological Survey of Western Australia, WA Geology Online, Explanatory Notes extract, viewed 22 June 2022, <www.dmirs.wa.gov.au/ens>.

Hickman, AH 2022b, Mallina Formation (A-CDm-s): Geological Survey of Western Australia, WA Geology Online, Explanatory Notes extract, viewed 22 June 2022, <www.dmirs.wa.gov.au/ens>.

Hickman, AH and Van Kranendonk, MJ 2012, Early earth evolution: evidence from the 3.5 – 1.8 Ga geological history of the Pilbara region of Western Australia: Episodes, v. 35, no. 1, p. 283–297, doi:10.18814/epiiugs/2012/v35i1/028.

Huston, DL, Champion, DC and Cassidy, KF 2014, Tectonic controls on the endowment of Neoarchean cratons in volcanic-hosted massive sulfide deposits: evidence from lead and neodynium isotopes: Economic Geology, v. 109, p. 11–26.

Huston, DL, Champion, DC, Ware, B, Carr, G, Maas, R and Tessalina, S 2019, Preliminary national-scale lead isotope maps of Australia: Record 2019/01, Geoscience Australia, Canberra, doi:10.11636/Record.2019.001.

Kerrich, R, Fryer, BJ, King, RW, Willmore, LM and van Hees, E 1987, Crustal outgassing and LILE enfichment in major lithosphere structures, Archean Abitibi greenstone belt: evidence on the source reservoir from strontium and carbon isotope traces: Contributions to Mineralogy and Petrology, v. 97, p. 156–168.

Kirk, J, Ruiz, J, Chesley, J, Walshe, J and England, G 2002, A major Archean gold- and crust-forming event in the Kaapval Craton, South Africa: Science, v. 297, p. 1856–1858.

Liu, H, Beaudoin, G, Makvandi, S, Jackson, SE and Huang, X 2021, Multivariate statistical analysis of trace element compositions of native gold from orogenic gold deposits: implication for mineral exploration: Ore Geology Reviews, v. 131, article no. 104061, doi:10.1016/j.oregeorev.2021.104061.

Maltese, A and Mezger, K 2020, The Pb isotope evolution of bulk silicate earth: constraints from its accretion and early differentiation history: Geochimica et Cosmochimica Acta, v. 271, p. 179–193.

Mathur, R, Titley, S, Ruiz, J, Gibbins, S and Friehauf, K 2005, A Re–Os isotope study of sedimentary rocks and copper–gold ores from the Ertsberg District, West Papua, Indonesia: Ore Geology Reviews, v. 26, no. 3–4, p. 207–226, doi:10.1016/j.oregeorev.2004.07.001.

McNaughton, NJ, Cassidy, KF, Dahl, N, Groves, DI, Perring, CS and Sang, JH 1990, Lead isotope studies, *in* Gold deposits of the Archaean Yilgarn Block, Western Australia: Nature, Genesis and Exploration Guides *edited by* EH Susan and JM Bennett: Geology Key Centre & University Extension, The University of Western Australia, Perth, Western Australia, p. 226–236.

McNaughton, NJ, Frost, KM and Groves, DI 1988, Ground melting and ocellar komatiites: a lead isotopic study at Kambalda, Western Australia: Geological Magazine, v. 125, no. 3, p. 285–295, doi:10.1017/S0016756800010220.

Morgan, JW and Wandless, GA 1980, Rare earth elements distribution in some hydrothermal minerals: evidence for crystallographic control: Geochimica et Cosmochimica Acta, v. 44, no. 7, p. 973–980, doi:10.1016/0016-7037(80)90286-0.

Mueller, AG, de Laeter, JR and Groves, DI 1991, Strontium isotope systematics of hydrothermal minerals from epigenetic Archean gold deposits in the Yilgarn Block, Western Australia: Economic Geology, v. 86, no. 4, p. 780–809, doi:10.2113/gsecongeo.86.4.780.

Mueller, AG, Hall, GC, Nemchin, AA, Stein, HJ, Creaser, RA and Mason, DR 2008, Archean high-Mg monzodiorite–syenite, epidote skarn, and biotite–sericite gold lodes in the Granny Smith–Wallaby district, Australia: U–Pb and Re–Os chronometry of two intrusion-related hydrothermal systems: Mineralium Deposita, v. 43, p. 337–362.

Park, J-W and Campbell, I 2020, Platinum-group element geochemistry of the volcanic rocks associated with the Jaguar and Bentley Cu–Zn volcanogenic massive sulfide (VMS) deposits, Western Australia: implications for the role of chalcophile element fertility on VMS mineralization: Mineralium Deposita, v. 56, p. 583–600, doi:10.1007/s00126-020-00991-9.

Rasmussen, B, Zi, J-W, Muhling, JR, Dunkley, DJ and Fischer, WW 2020, U–Pb dating of overpressure veins in late Archean shales reveals six episodes of Paleoproterozoic deformation and fluid flow in the Pilbara Craton: Geology, v. 48, no. 10, p. 961–965, doi:10.1130/G47526.1.

Rasmussen, B, Fletcher, IR, Muhling, JR, Thorne, WS and Broadbent, GC 2007, Prolonged history of episodic fluid flow in giant hematite ore bodies: Evidence from in situ U-Pb geochronology of hydrothermal xenotime: Earth and Planetary Science Letters, v. 258, p. 249–259.

Rimskaya-Korsakova, MN and Dubinin, AV 2003, Rare earth elements in sulphides of submarine hydrothermal vents of the Atlantic Ocean: Doklady Earth Sciences, v. 389A, no. 3, p. 432–436.

Rudnick, RL and Gao, S 2003, Composition of the continental crust: Treatise of Geochemistry, v. 3, p. 1–64.

Schaefer, BF, Pearson, DG, Rogers, NW and Barnicoat, AC 2010, Re–Os isotope and PGE constraints on the timing and origin of gold mineralisation in the Witwatersrand Basin: Chemical Geology, v. 276, no. 1–2, p. 88–94, doi:10.1016/j.chemgeo.2010.06.001.

Schupp, J 1985, Kurnalpi Project – preliminary geological report: Metana Minerals NL: Geological Survey of Western Australia, <www.dmirs.wa.gov.au/wamex>, 12p.

Selby, D and Creaser, RA 2003, Re–Os geochronology of organic rich sediments: an evaluation of organic matter analysis methods: Chemical Geology, v. 200, no. 3–4, p. 225–240, doi:10.1016/S0009-2541(03)00199-2.

Sener, AK, Young, C, Groves, DI, Krapež, B and Fletcher, IR 2005, Major orogenic gold episode associated with Cordilleran-style tectonics related to the assembly of Paleoproterozoic Australia: Geology, v. 33, p. 225–228.

Sheppard, S, Occhipinti, SA and Nelson, DR 2005, Intracontinental reworking in the Capricorn Orogen, Western Australia: the 1680– 1620 Ma Mangaroon Orogeny: Australian Journal of Earth Sciences, v. 52, p. 443–460.

Shirey, SB and Walker, RG 1995, Carius tube digestion for low-blank rhenium-osmium analysis: Analytical Chemistry, v. 67, no. 13, p. 2136–2141, doi:10.1021/ac00109a036.

Shirey, SB and Walker, RG 1998, The Re–Os isotope system in cosmochemistry and high-temperature geochemistry: Annual Review of Earth and Planetary Sciences, v. 26, p. 423–500, doi:10.1146/annurev.earth.26.1.423.

Stacey, JS and Kramers, JD 1975, Approximation of terrestrial lead isotope evolution by a two-stage model: Earth and Planetary Science Letters, v. 26, p. 207–221.

Sun, W, Benett, VC, Eggins, SM, Kamenetsky, VS and Arculus, R 2003, Enhanced mantle-to-crust rhenium transfer in undegassed arc magmas: Nature, v. 422, p. 294–297, doi:10.1038/nature01482.

Taylor, RN, Ishizuka, O, Michalik, A, Milton, JA and Croudace, IW 2015, Evaluating the precision of Pb isotope measurement by mass spectrometry: Journal of Analytical Atomic Spectrometry, v. 30, p. 198–213, doi:10.1039/C4JA00279B.

Thorpe, RI 1999, The Pb isotope linear array for volcanogenic massive sulfide deposits of the Abitibi and Wawa Subprovinces, Canadian Shield, *in* The Giant Kidd Creek Volcanogenic Massive Sulfide Deposit, Western Abitibi Subprovince, Canada *edited by* MD Hannington and CT Barrie: Society of Economic Geologists (SEG), Economic Geology Monograph 10, p. 555–576, doi:10.5382/Mono.10.25.

Thorpe, R, Hickman, AH, Davis, D, Morton, JGG and Trendall, AF 1992, U-Pb zircon geochronology of Archaean felsic units in the Marble Bar region, Pilbara Craton, Western Australia: Precambrian Research, v. 56, p. 169–189.

Vielreicher, N, Groves, D, McNaughton, N and Fletcher, I 2015, The timing of gold mineralization across the eastern Yilgarn Craton using U-Pb geochronology of hydrothermal phosphate minerals: Mineralium Deposita, v. 50, no. 4, p. 391–428.

Witt, W, Cassidy, K, Lu, Y-J and Hagemann, S 2018, Syenitic group intrusions of the Archean Kurnalpi Terrane, Yilgarn Craton: hosts to ancient alkali porphyry gold deposits: Ore Geology Reviews, v. 96, p. 262–268, doi:10.1016/j.oregeorev.2017.08.037.

Woodhead, JD, Volker, F and McCulloch, MT 1995, Routine lead isotope determinations using a lead-207–lead-204 double spike: a long-term assessment of analytical precision and accuracy: Analyst, v. 120, p. 35–39, doi:10.1039/AN9952000035.

REPORT
229

# ISOTOPIC FINGERPRINTING OF NATIVE GOLD FROM WESTERN AUSTRALIA

SG Tessalina, EA Hancock, B Ware and NJ McNaughton

The aim of this Report is to investigate applicability of thermal ionization mass spectrometry (TIMS) and high-resolution inductively coupled plasma mass spectrometry (HR-ICP-MS) in combination with wet chemistry for isotopic and sub-ppb trace element fingerprinting of native gold grains and, therefore, for constraining the age and source of gold mineralization. Twenty-four placer and primary gold samples from the Pilbara Craton, Kurnalpi Terrane and Capricorn Orogen in Western Australia were analysed for Pb and Os isotopes, platinum group elements (PGE) and other trace elements.

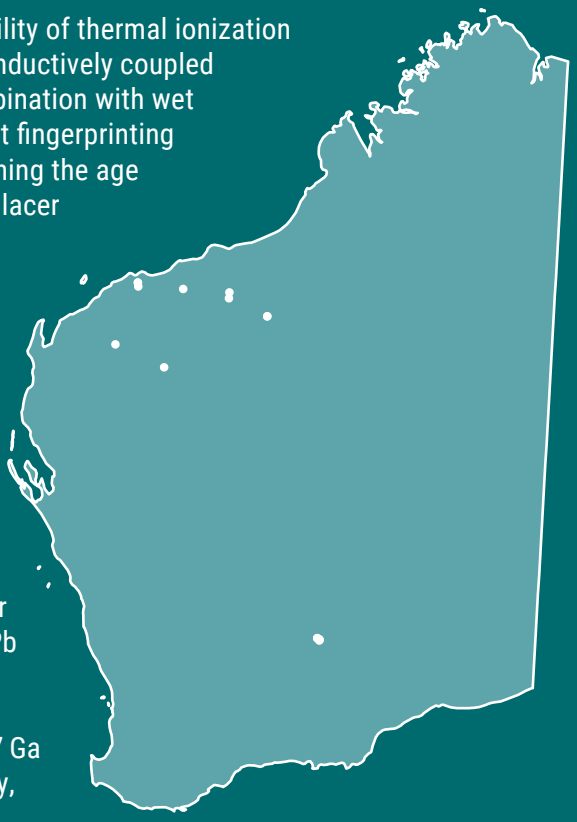

The results for the established Pb–Pb model ages for gold grains and their galena inclusions show that small nuggets from the Kurnalpi Terrane display the most primitive Pb isotope compositions, with Neoarchean model ages ranging from 2.72 to 2.65 Ga, similar to ages of the host rocks. The least radiogenic Pb isotopes from galena inclusions in Pilbara gold yield model ages of 2.25 Ga for Marble Bar, 2.66 – 2.44 Ga for Mosquito Creek and 2.91 – 2.87 Ga for Silica Hills, indicating a more complex history, possibly due to overprinting by younger events. Gold samples from Capricorn Orogen deposits show no evidence of alteration or overprinting by geological events since their formation. A gold nugget from the Mount Olympus area yielded a model age of 1.66 Ga, which is compatible with the known age of the younger mineralization event at the Paulsens gold mine.

The source μ ($^{238}U/^{204}Pb$) values for galena inclusions and less-altered gold nuggets from the Kurnalpi Terrane are similar to values for volcanogenic massive sulfide deposits at Teutonic Bore and Nimbus, indicating a mostly juvenile, predominantly mantle-derived source for Pb. The Re–Os systematics of gold reveal also a mantle source of Os, possibly related to magmatic fluid input without significant crustal contamination. The Re–Os and PGE patterns in placer gold nuggets from the Pilbara appear to preserve their initial source signatures without significant chemical alteration during their burial history.

Further details of geoscience products are available from:

First Floor Counter
Department of Mines, Industry Regulation and Safety
100 Plain Street
EAST PERTH WESTERN AUSTRALIA 6004
Phone: +61 8 9222 3459 Email: publications@dmirs.wa.gov.au
www.dmirs.wa.gov.au/GSWApublications